Miner Deposita (2016) 51:725–748
DOI 10.1007/s00126-015-0633-9

ARTICLE

The Marianas-San Marcos vein system: characteristics of a shallow low sulfidation epithermal Au–Ag deposit in the Cerro Negro district, Deseado Massif, Patagonia, Argentina

Conrado Permuy Vidal[1] · Diego M. Guido[1] · Sebastián M. Jovic[1] · Robert J. Bodnar[2] · Daniel Moncada[3] · Joan Carles Melgarejo[4] · Willis Hames[5]

Received: 6 July 2015 / Accepted: 16 December 2015 / Published online: 18 January 2016

Abstract The Cerro Negro district, within the Argentinian Deseado Massif province, has become one of the most significant recent epithermal discoveries, with estimated reserves plus resources of ~6.7 Moz Au equivalent. The Marianas-San Marcos vein system contains about 70 % of the Au–Ag resources in the district. Mineralization consists of Upper Jurassic (155 Ma) epithermal Au- and Ag-rich veins of low to intermediate sulfidation style, hosted in and genetically related to Jurassic intermediate composition volcanic rocks (159–156 Ma). Veins have a complex infill history, represented by ten stages with clear crosscutting relationships that can be summarized in four main episodes: a low volume, metal-rich initial episode (E1), an extended banded quartz episode with minor mineralization (E2), a barren waning stage episode (E3), and a silver-rich late tectonic–hydrothermal episode (E4). The first three episodes are interpreted to have formed at the same time and probably from fluids of similar composition: a 290–230 °C fluid dominated by meteoric and volcanic waters (−3‰ to −0‰ $\delta^{18}O_{water}$), with <3 % NaCl equivalent salinity and with a magmatic source of sulfur (−1 to −2 ‰ $\delta^{34}S_{water}$). Metal was mainly precipitated at the beginning of vein formation (episode 1) due to a combination of boiling at ~600 to 800 m below the paleowater table, and associated mixing/cooling processes, as evidenced by sulfide-rich bands showing crustiform-colloform quartz, adularia, and chlorite-smectite banding. During episodes 2 and 3, metal contents progressively decrease during continuing boiling conditions, and veins were filled by quartz and calcite during waning stages of the hydrothermal system, and the influx of bicarbonate waters (−6 to −8.5 ‰ $\delta^{18}O_{water}$). Hydrothermal alteration is characterized by proximal illite, adularia, and silica zone with chlorite and minor epidote, intermediate interlayered illite-smectite and a distal chlorite halo. This assemblage is in agreement with measured fluid inclusion temperatures. A striking aspect of the Marianas-San Marcos vein system is that the high-grade/high-temperature veins are partially covered by breccia and volcaniclastic deposits of acidic composition, and are spatially associated with hot spring-related deposits and an advanced argillic alteration blanket. A telescoped model is therefore proposed for the Marianas-San Marcos area, where deeper veins were uplifted and eroded, and then partially covered by non-explosive, post-mineral rhyolitic domes and reworked volcaniclastic deposits, together with shallow geothermal features. The last tectonic–hydrothermal mineralization episode (E4), interpreted to have formed at lower temperatures, could be related to this late tectonic and hydrothermal activity.

Editorial handling: F. Barra

Electronic supplementary material The online version of this article (doi:10.1007/s00126-015-0633-9) contains supplementary material, which is available to authorized users.

✉ Conrado Permuy Vidal
conradopermuyvidal@gmail.com

[1] CONICET and Facultad de Ciencias Naturales y Museo, Instituto de Recursos Minerales (INREMI), Universidad Nacional de La Plata, Calle 64 y 120, B1900FWA La Plata, Argentina

[2] Department of Geosciences, Virginia Tech, Blacksburg, VA 24061, USA

[3] Department of Geology and Andean Geothermal Center of Excellence (CEGA), Universidad de Chile, Plaza Ercilla 803, Santiago, Chile

[4] Departament de Cristalografia, Mineralogia i Dipòsits Minerals, Facultat de Geologia, Universitat de Barcelona, Martí i Franquès, s/n, 08028 Barcelona, Spain

[5] Department of Geosciences, Auburn University, Auburn, AL 36849, USA

Keywords Epithermal · Quartz vein · Jurassic · Patagonia · Argentina

Introduction

The Cerro Negro district is located at the northwestern margin of the Deseado Massif geological province, Patagonia, Argentina (Fig. 1). The area has been the focus of exploration by several mining companies since the 1990s, and hosts numerous epithermal gold and silver deposits related to Jurassic volcanism, leading Schalamuk et al. (1999) to define the region as an Au–Ag metallogenic province. Since ~2000, the region has produced 4.9 Moz of gold and over 100 Moz of silver from six mines: Cerro Vanguardia, Martha (currently inactive), Manantial Espejo, San José, Lomada de Leiva, and Cerro Negro (opened in 2014, and the focus of this study). These mines, as well as more than 50 epithermal projects in various stages of exploration, document the significant economic potential of the region (Fig. 1).

Deseado Massif epithermal deposits include low to intermediate sulfidation veins, stockworks, and breccias (Guido and Schalamuk 2003; Echavarría et al. 2005; Fernández et al. 2008), controlled by major NW to WNW Jurassic rift structures and minor NE and E–W trending structures (Giacosa et al. 2010; Páez et al. 2016). The region also records several Jurassic geothermal paleosurface features, such as silica and carbonate hot spring deposits, with associated steam-heated advanced argillic alteration and phreatic breccias (Schalamuk et al. 1997, 1999; Guido et al. 2002; Echeveste 2005; Channing et al. 2007; Guido and Campbell 2011, 2012, 2014). Geochronological data reveal that the hydrothermal systems formed during restricted episodes within the long-lived and widespread Jurassic extensional event (Arribas et al. 1996; Schalamuk et al. 1997, 2002; Guido and Schalamuk 2003; Echavarría et al. 2005).

The Cerro Negro district comprises a large (~26,500 ha) area that was explored by several companies since the early 1990s. After more than 15 years of exploration, Andean Resources demonstrated economic mineralization, and the property was acquired by Goldcorp mining company in 2010. Current proven reserves consist of 5.74 Moz of gold and 49.36 Moz of silver, with additional probable resources of 0.82 Moz of gold and 5.87 Moz of silver (www.goldcorp.com). Production began during mid-2014 and total gold production during 2014 was 152,000 oz. The majority of the resource is hosted by the Eureka vein and the Marianas-San Marcos vein systems (Fig. 2), which are located in the western part of the Cerro Negro district. The mineralization is hosted in steeply dipping epithermal Au- and Ag-rich veins with exceptional widths and lengths (Shatwell et al. 2011).

This paper summarizes the mineralogical, textural, and fluid characteristics of the Marianas-San Marcos vein system, consisting of the Mariana Central, Mariana Norte, and San Marcos quartz veins. Observations are supported by detailed petrographic examination of veins and hydrothermal alteration, detailed mineralogical studies, geochronology, fluid inclusions, and stable isotope analysis. These data contribute to a clear understanding of the different mineralization stages forming the veins, their relative importance considering the total Au–Ag resource, and a detailed definition of the fluid evolution and metal precipitation mechanism for those stages

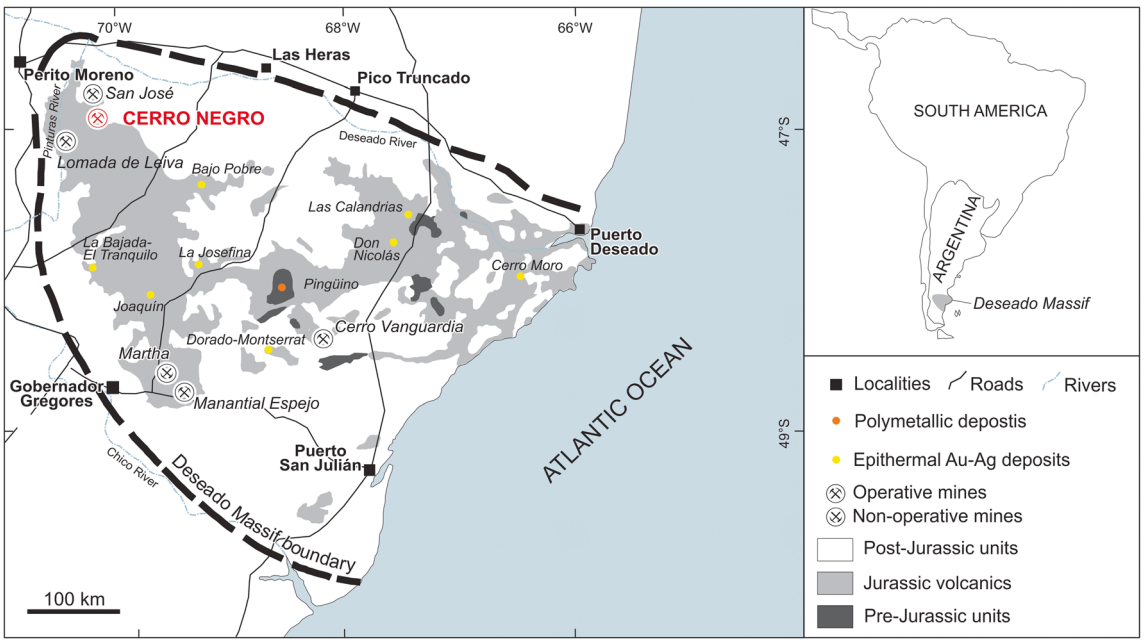

Fig. 1 Simplified geological map of the Deseado Massif, showing the distribution of Jurassic volcanic rocks and the location of the Au–Ag mines and significant epithermal projects

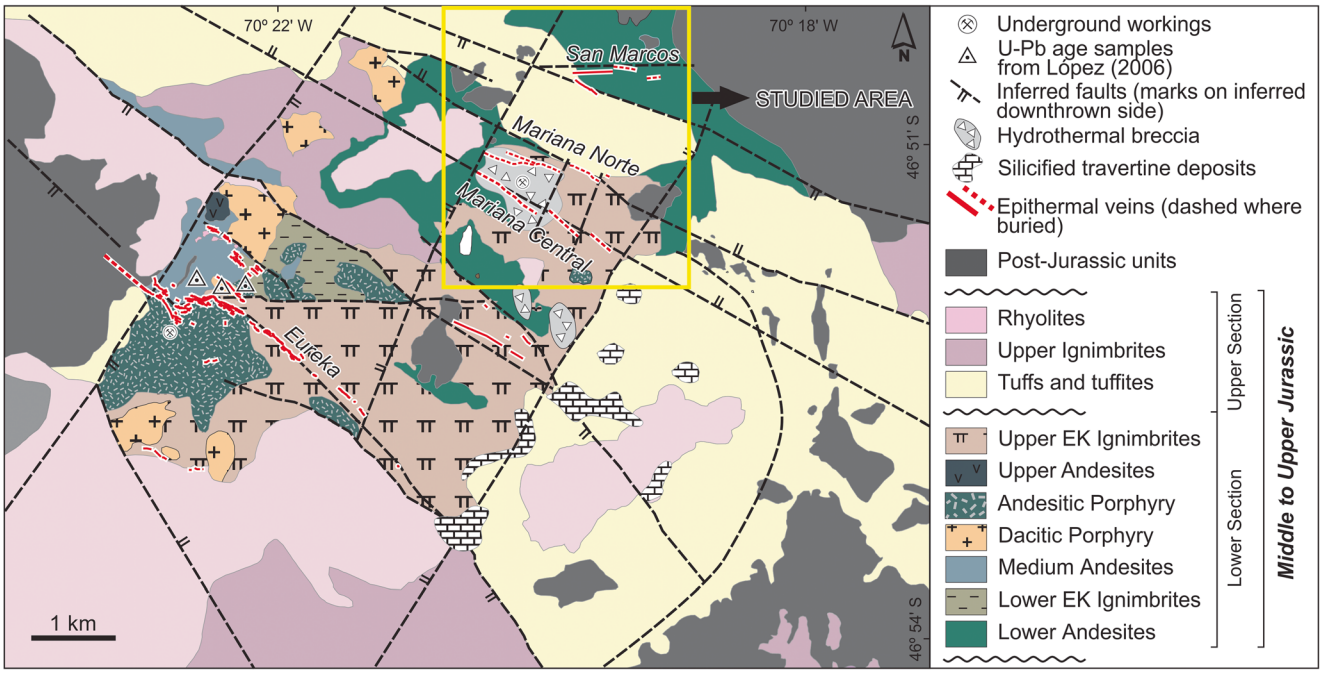

Fig. 2 Geological map of the western part of the Cerro Negro district, showing the Marianas-San Marcos study area. Modified from Lopez (2006) and Guido and Campbell (2012)

providing the Au–Ag grade. All information has been integrated to develop a geological and mineralization model for the Marianas-San Marcos vein system, consistent with diagnostic features of the outcropping shallow epithermal environment and related to the evolution of Jurassic volcanism in the region.

Sampling and analytical techniques

The Marianas-San Marcos vein system was studied using drill core from more than 50 representative drill holes on the main vein structures. The samples represent different levels in the vein system and the full range of precious metal grades in order to document spatial and temporal variations (Figs. 3 and 4). A total of 373 samples, covering all stages of mineralization observed in drill holes, were collected for further study using petrography, SEM-EDS, electron microprobe, compilation of available geochemical data, X-ray diffraction, fluid inclusions, stable isotopes, and geochronology.

Gangue and ore petrography was carried out at the Instituto de Recursos Minerales, La Plata, Argentina. Electron microscope imaging and microprobe analysis of minerals in polished thin sections were carried out at the Departamento de Cristalografía, Mineralogía y Depósitos Minerales, Universidad de Barcelona, Spain (ESM 1). X-ray diffraction analyses of clay alteration minerals (ESM 2) were performed at the Centro de Investigaciones Geológicas, La Plata, Argentina (CIG-CONICET).

$^{40}Ar/^{39}Ar$ ages from vein adularia were determined at Auburn University (USA). For each sample slab, a diamond core drill was used to obtain one or two cores (10 and 5 mm diameter) of material rich in adularia (ESM 3). One core piece was then crushed with a mortar and pestle, and individual pieces were selected under a binocular microscope for analysis. Four of the samples contained adularia sufficiently coarse for single crystal analysis (#95048, #91590, #96335, #111082), whereas the pieces selected from two samples (#102017 and #100932) were aggregates of fine adularia intergrown with quartz. Samples thus prepared were irradiated in the USGS TRIGA reactor in Denver, CO, with Fish Canyon sanidine (FC-2) as the flux monitor. The *J* value for all samples is 0.006019 ± 0.0000060 (at 1σ). Samples were analyzed in the Auburn Noble Isotope Mass Analysis Lab (ANIMAL) facility at Auburn University. Argon was extracted by heating with a CO_2 laser, using two different methods: first, five analyses of a given sample were obtained by fusing single crystals to obtain a general probability distribution and mean of single crystal ages for that sample. The second strategy was to incrementally heat a relatively large crystal (or aggregate piece) and obtain a spectrum of ages for the sample. The first strategy allows assessment of the distribution of age for a population, whereas the second strategy is more effective for discerning effects of extraneous argon or loss of radiogenic argon that might affect the sample. Both types of data were plotted on typical incremental heating diagrams. In cases of fusion results with scatter significantly beyond precision, an average age and uncertainty were obtained by adding a constant error to each data point. Data were statistically reduced with the

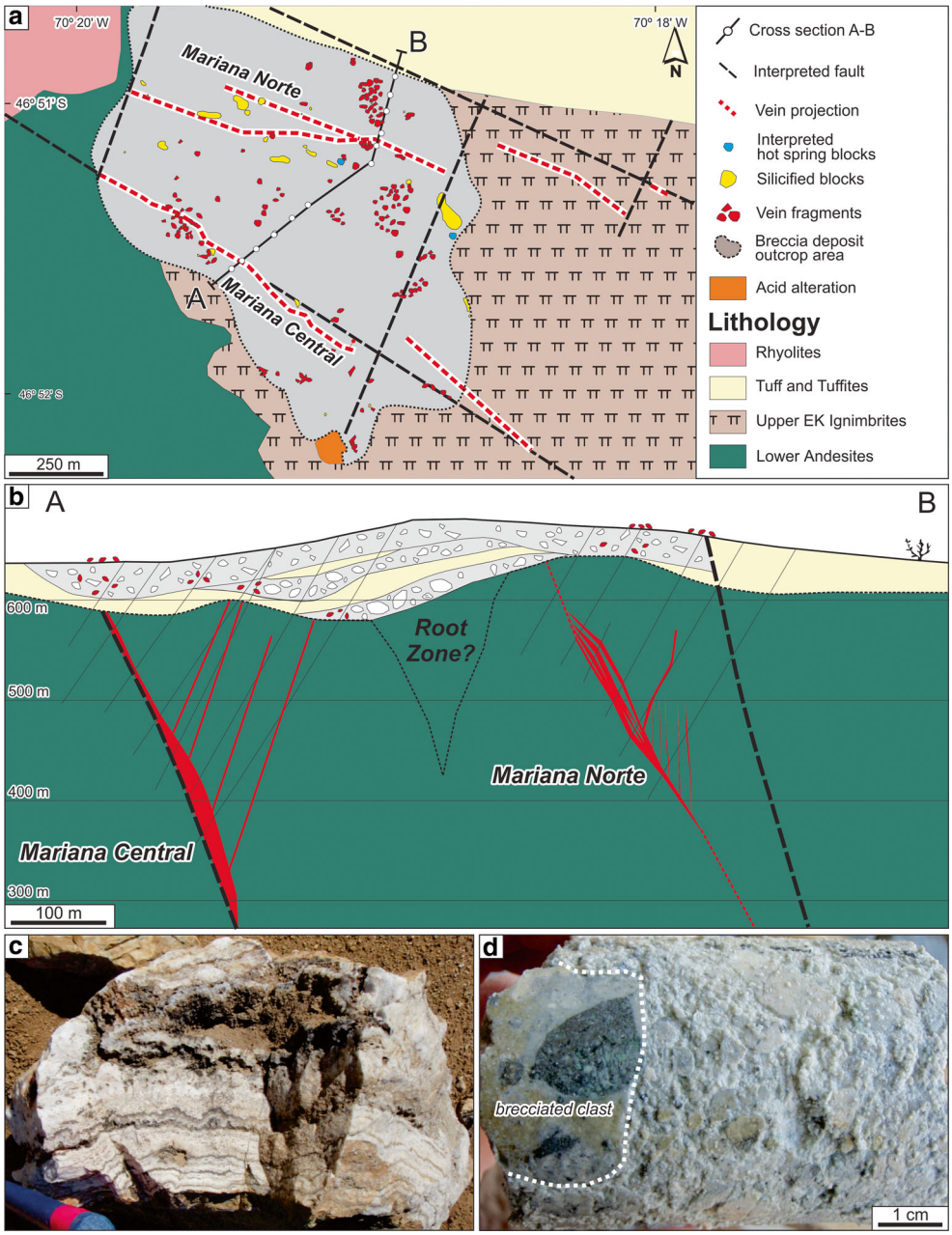

Fig. 3 Marianas vein area. **a** Plan view. **b** Interpreted *A–B* section along the post-mineralization breccia deposit. **c** Banded quartz vein fragment at the breccia surface. **d** Breccia clast (*dotted line*) in muddy clay-rich matrix polymictic breccia

program Isoplot (Ludwig 2001). Other details of the analytical data are provided in the data table from ESM 3.

Microscopy and microthermometric studies on fluid inclusions (FI) from the veins were carried out with a Linkam freezing/heating stage at the Fluid Inclusion Laboratory of Virginia Tech (USA). Doubly polished sections were prepared from 21 drill core samples covering representative stages from the Marianas-San Marcos veins, and described following criteria outlined in Roedder (1984) and Goldstein and Reynolds (1994). Fluid salinity was estimated from final ice-melting temperatures (T_m) using phase equilibria in the NaCl-H_2O model system (Bodnar 1993). Raman spectroscopy was used to test for the presence of CO_2 in vapor-rich inclusions and to identify solid phases in FI, using a Jobin-Yvon Horiba LabRam Raman microprobe in the Fluids Research Laboratory at Virginia Tech. In the same laboratory, selected inclusions were analyzed by laser ablation inductively coupled plasma mass spectrometry (LA-ICP-MS) using a Microlas 193 nm Ar ion excimer laser coupled with an Agilent quadrupole mass spectrometer. Elements included in the analytical menu were Na, Mg, K, Ca, Mn, Fe, Cu, Zn, Pb, Ag, Au, As, Sb, Se, and Te. The NIST610 glass standard was used for calibration (see Heinrich et al. 2003). Sample reduction was developed with AMS software (Mutchler et al. 2008).

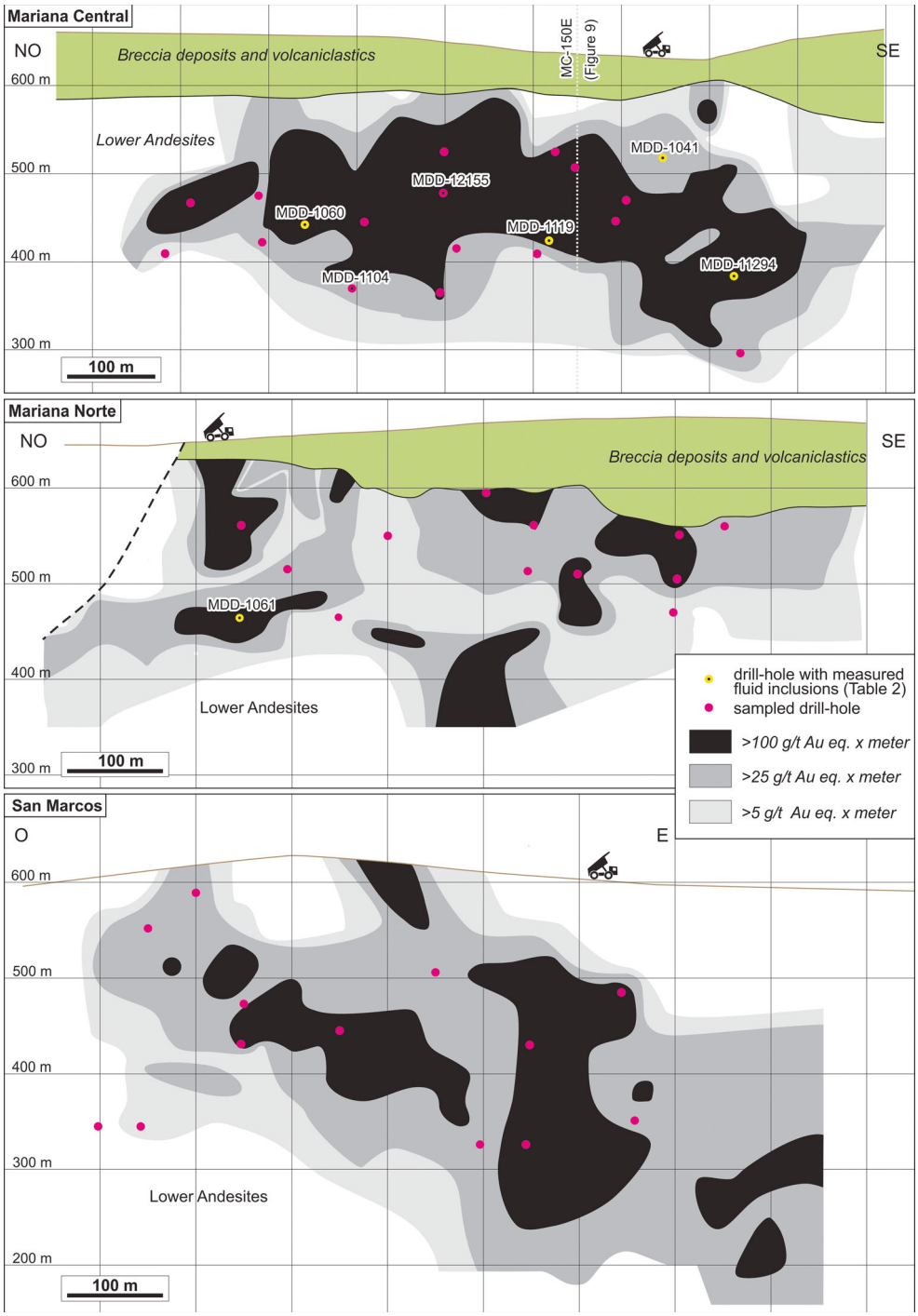

Fig. 4 Longitudinal sections of the Mariana Central, Mariana Norte, and San Marcos veins (modified from www.goldcorp.com) with location of drill-holes samples for this study

Representative samples from specific mineralization stages were selected for stable isotope studies (oxygen, hydrogen, carbon, and sulfur). Samples were prepared at Activation Laboratories (Actlabs), in Canada, following the procedures described in Clayton and Mayeda (1963) and Ueda (1986) and analyzed with Finnigan MAT Delta, VG SIRA-10 and VG 602 stable isotope ratio mass spectrometers. The data are reported in the standard delta notation as per mil deviations from V–SMOW for oxygen and deuterium, the VPDB standard for carbon, and the VCDT standard for sulfur isotopic compositions.

Regional geology

The Deseado Massif is part of the Chon Aike Large Igneous Province of Middle to Upper Jurassic age (Pankhurst et al. 1998, 2000). This volcanic mega-event occurred over a period

of ~30 Ma, in an extensional setting interpreted as a diffuse back-arc environment related to the early break-up of Gondwana and the opening of the South Atlantic Ocean (Riley et al. 2001; Ramos 2002; Richardson and Underhill 2002). Within the Deseado Massif geological province (Fig. 1), the Bahía Laura Volcanic Complex (BLVC) (Feruglio 1949; Guido 2004) is the most relevant unit, and includes the Bajo Pobre, Cerro León, Chon Aike, and La Matilde formations showing complex interfingering of the different facies (Echeveste et al. 2001; Guido et al. 2006; Ruiz 2012). These formations comprise the Jurassic volcanics within the Deseado Massif province (Fig. 1), constituting about 60 % of the outcrops.

The Bajo Pobre Formation consists of intermediate to basic, calc-alkaline volcanic, and volcaniclastic rocks, mostly of andesite composition. The subvolcanic equivalent is represented by the Cerro León Formation (de Barrio et al. 1999; Panza and Haller 2002; Jovic et al. 2008). The Chon Aike Formation is dominantly composed of silicic ignimbrites (about 90 % of the outcrops), with subordinate reworked volcaniclastic deposits, air fall tuffs, intercalated lavas, dikes, and rhyolitic domes (Pankhurst et al. 1998, 2000; Riley et al. 2001; Sharpe et al. 2002; Panza and Haller 2002). The top of the Jurassic sequence is dominated by the La Matilde Formation, characterized by a homogeneous sequence of reworked volcaniclastic sediments formed in low-energy fluvial and lacustrine settings, with minor intercalations of ash fall tuffs and ignimbrites (de Barrio et al. 1999). Chon Aike and La Matilde Formations were interpreted to form the Bahía Laura Group (Lesta and Ferello 1972; Hechem and Homovc 1987), a stratigraphic term that is not compatible with the volcanic complex.

District geology

The western part of the Cerro Negro district is characterized by a 500-m-thick Jurassic volcanic sequence (Fig. 2) that uncomfortably overlies a Paleozoic low-grade metamorphic basement that is not exposed at the surface, and was found with drilling (Permuy Vidal et al. 2014). Locations of volcanic rocks are controlled by major WNW (N 290° to N 310°) and minor EW and NE (N 10°) structures that define the margins of graben structures filled by the volcanic rocks (Shatwell et al. 2011). Based on field relationships, composition and ages, the Middle to Upper Jurassic volcanic units were grouped into Lower and Upper Sections (Fig. 2).

The Lower Section starts with a series of andesitic lava flows named Lower Andesites that crop out in the central to northeast part of the area and constitute the main host rock of the Marianas-San Marcos vein system. This unit was intercepted at depths of ≤500 m during drilling (Fig. 2). Andesites are characterized by porphyritic texture with plagioclase and pyroxene phenocrysts in a pilotaxic to felsitic groundmass with abundant vesicles. To the west, and toward the northwestern part of Eureka vein, these lava flows are overlain by a package of welded ignimbrites of dacitic composition of the Lower EK Ignimbrite unit, and then by the Medium Andesite, another porphyritic plagioclase, pyroxene andesitic flow. For the last unit, the Medium Andesite, Lopez (2006) reports a U–Pb zircon age of 159 ±2.1 Ma from a sample located in the northern portion of the Eureka vein (Fig. 2 and ESM 4).

The volcanic sequence described above is intruded by two porphyritic bodies: a K-feldspar, hornblende and biotite phenocryst-rich dacite, and a plagioclase and pyroxene phenocryst-rich andesite. U–Pb ages of 157 ± 1.7 Ma for the dacitic and 156 ± 1.2 Ma for the andesitic porphyry were obtained by Lopez (2006) from these intrusions that outcrop in the northern part of the Eureka vein (Fig. 2 and ESM 4). The Lower Section is topped by aphanitic lava flows of the Upper Andesite unit, and the widespread unwelded dacitic pyroclastic flow of the Upper EK Ignimbrite (Fig. 2).

A district-wide disconformity is clearly recognized in the study area, and separates the Lower Section from a new volcanic event, the Upper Section volcanic units (Fig. 2). The Upper Section consists of thick unwelded widespread ignimbrites, tuffs and surge deposits, and rhyolitic domes of the Tuffs and Tuffites, Upper Ignimbrite and Rhyolite units (Fig. 2). The Upper Section is dominated by tuffaceous rocks developed within an extensive fluvio-lacustrine environment with travertine-depositing hot springs that are interpreted to have developed during the waning stages of this acidic volcanism (Guido and Campbell 2012).

In a broad sense, the lithological descriptions of the Lower Section can be assigned to the Bajo Pobre Formation, while the Upper Section can be related to the Bahía Laura Group (Chon Aike and La Matilde formations). Moreover, ages for the Lower Section units (159 to 156 Ma) are in agreement with the available geochronological data for the Bajo Pobre Formation in the western Deseado Massif (160 to 150.6 Ma, Table 1). Based on field relationships, the Upper Section should be younger than 156 Ma, and can be correlated with the youngest reported ages for the Chon Aike Formation (154.6 to 147.6 Ma, Table 1) at the Río Pinturas and San José District, western Deseado Massif.

In the study area, the principal epithermal Au–Ag vein systems (Eureka and the Marianas-San Marcos vein system) are emplaced within the Lower Section units, and are hosted by WNW and EW structures, related to a major NNW (N 340°) striking sinistral strike-slip fault system located in the northwestern corner of the Deseado Massif (Lopez et al. 2002; Dietrich et al. 2012). The high-grade Au–Ag mineralization is buried by post-mineral deposits of the Upper Section (Figs. 2,

Table 1 Summary of geochronological data of volcanic units and mineralization from western Deseado Massif

Location	Unit/Vein	Lithology/Mineral	Method	Age (Ma)	References
Bajo Pobre	Bajo Pobre Formation	Andesitic lava	Ar-Ar	156.7 ± 4.6	Alric et al. (1996)
Bajo Pobre	Bajo Pobre Formation	Andesitic lava	Ar-Ar	152.7 ± 1.2	Féraud et al. (1999)
Bajo Pobre	Bajo Pobre Formation	Andesitic lava	Ar-Ar	152.8 ± 2.6	Féraud et al. (1999)
Manantial Espejo	Bajo Pobre Formation	Quartz andesite	U/Pb SHRIMP (Zircon)	156.7 ± 1.3	Wallier (2009)
Manantial Espejo	Bajo Pobre Formation	Andesitic lava	U/Pb SHRIMP (Zircon)	160.0 ± 1	Wallier (2009)
Manantial Espejo	Bajo Pobre Formation	Andesite porphyry	U/Pb SHRIMP (Zircon)	160.0 ± 1.2	Wallier (2009)
Manantial Espejo	Chon Aike Formation	Rhyolitic Ignimbrite	Ar-Ar	157.9 ± 0.5	Féraud et al. (1999)
Manantial Espejo	Chon Aike Formation	Rhyolitic Ignimbrite	Ar-Ar	158.4 ± 0.3	Féraud et al. (1999)
Manantial Espejo	Chon Aike Formation	Rhyolitic Ignimbrite	U/Pb SHRIMP (Zircon)	161.5 ± 0.8	Wallier (2009)
Manantial Espejo	Chon Aike Formation	Dacitic Ignimbrite	U/Pb SHRIMP (Zircon)	162.0 ± 0.8	Wallier (2009)
Manantial Espejo	Chon Aike Formation	Ignimbrite	U/Pb (Zircon)	159.9 ± 0.5	Dubé et al. (2003)
Mina Martha	Bajo Pobre Formation	Dacitic lava	Ar-Ar	156.9 ± 0.7	Ruiz (2012)
Mina Martha	Chon Aike Formation	Rhyodacitic Ignimbrite	Ar-Ar	157.6 ± 1	Ruiz (2012)
Río Pinturas	Chon Aike Formation	Ignimbrite	Ar-Ar	151.5 ± 1	Alric et al. (1996)
Río Pinturas	Chon Aike Formation	Rhyolitic Ignimbrite	Ar-Ar	153.4 ± 0.3	Féraud et al. (1999)
Río Pinturas	Chon Aike Formation	Rhyolitic Ignimbrite	Ar-Ar	154.6 ± 0.5	Féraud et al. (1999)
San José District	Bajo Pobre Formation	Volcaniclastic unit	Ar-Ar	150.6 ± 4.1	Dietrich et al. (2012)
San José District	Bajo Pobre Formation	Andesitic lava	Ar-Ar	151.3 ± 0.7	Dietrich et al. (2012)
San José District	Chon Aike Formation	Rhyodacitic Ignimbrite	Ar-Ar	147.6 ± 1.1	Dietrich et al. (2012)
Manantial Espejo	María Vein	Adularia	Ar-Ar	153.5 ± 0.8	Wallier (2009)
Manantial Espejo	María Vein	Adularia	Ar-Ar	154.2 ± 0.9	Wallier (2009)
Manantial Espejo	María Vein	Adularia	Ar-Ar	154.0 ± 0.8	Wallier (2009)
Manantial Espejo	María Vein	Adularia	Ar-Ar	156.6 ± 0.8	Wallier (2009)
Manantial Espejo	Concepción Vein	Adularia	Ar-Ar	154.2 ± 0.9	Wallier (2009)
Manantial Espejo	Mesa Vein	Adularia	Ar-Ar	152.8 ± 0.8	Wallier (2009)
Manantial Espejo	Mesa Vein	Adularia	Ar-Ar	155.5 ± 0.9	Wallier (2009)
Mina Martha	Catalina Vein	Adularia	Ar-Ar	156.5 ± 0.9	Páez et al. (2016)
San José District	Huevos Verdes	Adularia	Ar-Ar	151.2 ± 0.5	Dietrich et al. (2012)

3, and 4). In the Eureka vein, a high-grade Au–Ag ore-shoot extends below the post-mineral unconformity and is overlain by younger reworked pyroclastic volcanic rocks of the Upper Section, as noted by Lopez (2006) and Shatwell et al. (2011).

In the Marianas-San Marcos area, thick breccia deposits and reworked volcanic rocks buried the mineralized structures (Figs. 3 and 4a, b). The breccia deposits exhibit a sub-circular 600 by 350 m depression with clasts up to 2 m in diameter lying on the surface (Fig. 3a–c). Surface mapping shows that breccia blocks are composed of hydrothermally altered host rocks, silicified breccias, silicified travertine deposits, and mineralized vein clasts that are distributed above and close to the hidden veins. High-grade clasts in the breccias were the key to discovering blind Marianas veins (Shatwell et al. 2011, Fig. 3b). At depth, the breccia is polymictic, matrix-supported, and composed by angular to sub-angular, variably-sized clasts (Fig. 3d). The matrix mostly consists of comminuted rock flour material with abundant greenish tinted clays (smectite) and late thin calcite and gypsum veinlets. The size and abundance of banded vein fragments increases toward and above mineralized veins. The breccia deposits are interbedded with up to 20 m of reworked volcaniclastic deposits of the Tuff and Tuffite unit (Fig. 3b), with a subtle calcite alteration, and without vein fragments (Permuy Vidal et al. 2013).

The Marianas-San Marcos vein system

The Marianas-San Marcos epithermal vein system occupies major WNW–NW and EW normal faults related to a half-graben structure (Figs. 2 and 3). Veins are mostly developed in the Lower Andesite unit and to a minor extent in the Upper EK Ignimbrite. Veins are characterized by a Ag/Au ratio of about 10, less than 3 wt.% base metal content, and anomalous concentrations of As, Sb, Se, Hg, and Tl (Table 2).

Table 2 Summary of geochemical data of the Marianas-San Marcos vein system

	n	Au (g/t)		Ag (g/t)		*n*	BM (%)[a]		As (g/t)		Sb (g/t)		Se (g/t)		Hg (g/t)		Tl (g/t)	
		Av	Max	Av	Max		Av	Max	Av	Max	Av	Max	Av	Max	Av	Max	Av	Max
Mariana Central	2414	17.7	1261	119	10,232	1165	0.05	2.76	19.9	449	4.97	301	1.59	69.4	0.04	1.25	0.10	4.2
Mariana Norte	2828	10.4	2683	56.3	2844	2157	0.03	0.99	72.7	3536	4.80	182	1.30	53.0	0.08	4.28	0.17	4.2
San Marcos	2806	9.6	668	86	2770	1435	0.02	0.45	67.5	1166	6.98	602	2.84	73.9	0.18	12.4	0.30	0.3

n number of samples

[a] BM = Pb + Zn + Cu

The Mariana Central and Mariana Norte veins represent about ~50 % of the resources in the district (3.3 Moz Au equiv.). These two veins do not crop out, and were discovered beneath the post-mineral breccia deposits and reworked volcaniclastics during a fence-drilling program (Shatwell et al. 2011; Permuy Vidal et al. 2013). Marianas veins are NW–WNW trending, dip steeply (60° to 80°) to the northwest, with the Mariana Norte vein at N 260° and Mariana Central at N 305° azimuth (Figs. 2 and 3). Mariana Central consists of a main wide structure, with sub-parallel discontinuous footwall and hanging-wall splays. The vein is 950-m long and extends to a depth of 400 m. It has an average width of 5 m, reaching a maximum of 20 m, with the highest Au–Ag grades (>100 g/t Au eq. per meter) contained in a 100-m-thick sub-horizontal layer that extends along the vein strike for about 750 m (Fig. 4a), suggesting normal faulting as the main structural control during ore deposition. Mariana Norte consists of a tabular WNW trending structure with hanging-wall splays. Exploration drilling defined a main structure extending 850 m in strike-length, with an average width of 3.5 m, reaching up to ~10 m, and with irregularly distributed and smaller ore shoots (about 100 by 100 m) with >100 g/t Au eq. per meter (Fig. 4b). The ore shoots may indicate a more complex expression of veins that formed during or after ore deposition. The San Marcos vein occupies a dilatational E–W fault of the major NW striking and south-dipping San Marcos Sur fault. The vein dips 85–90° (subvertical) with a slight north dip in the western portion and a slight southward dip in eastern portion. Mineralization has been proven for 800 m along strike and to a depth of 400 m, with an average width of 4 m and extending up to 15 m. The ore shoots have gentle to steep easterly plunge (Fig. 4c), suggesting a strike-slip environment during mineralization.

Vein paragenesis, mineralogy, and textures

The Marianas-San Marcos vein system was developed during a complex history of vein filling, with ten mineralization stages identified based on crosscutting relationships. These stages were grouped into four main episodes according to mineralogical assemblages and metal contents (Fig. 5).

Episode 1

The first episode (E1) is composed of four stages. The first stage (S1) consists of early tabular adularia crystals intergrown with coarse quartz, followed by a fine-grained quartz-adularia colloform-crustiform banding with clays (ESM 2) and sulfide-rich bands and patches where precious metals can reach up to 1000 ppm Au and 10,000 ppm Ag in less than 1-m width (Figs. 5, 6a, and 7b). Quartz shows diverse textures that reveal partial to almost complete recrystallization from former chalcedony or amorphous silica (mosaic, moss, ghost-spheres, flamboyant, and "dusty quartz"). Also, massive quartz intergrown with lattice texture (parallel bladed) after platy calcite is present. Quartz bands alternate with a rhombic adularia and greenish clay-rich bands composed of chlorite-smectite (Figs. 5 and 6a), with later quartz typified by coarser crystals of amethyst. Clays of the same composition accompanied by kaolinite also occur crosscutting the vein banding and as breccias that probably formed later (Fig. 6a). The early-formed ore minerals include pyrite, chalcopyrite, Fe-poor sphalerite, and minor galena, followed by acanthite and polybasite-pearceite with Se contents up to 4.7 % (Figs. 5 and 7c; ESM 1). Minor amounts of associated tetrahedrite and pyrargyrite occur in this stage. The late ore forming minerals are composed of massive chalcopyrite accompanied by electrum, with a mean Au content of 60 % (Figs. 5 and 7d; ESM 1).

The second stage (S2) is characterized by delicate colloform chalcedony (now partially recrystallized to quartz) and adularia banding (Figs. 5 and 6b, c) with quartz lattice texture after platy calcite and a characteristic replacement texture after pseudoacicular minerals (Figs. 5, 6c, and 7e). Those replacements are similar to habits of zeolite group minerals described by Simpson and Mauk (2011) for low sulfidation epithermal veins in New Zealand. Fewer clay-rich bands are observed, compared to stage 1, and they are composed of chlorite-smectite, illite, and kaolinite. Ore minerals also decrease in abundance with respect to S1, and are represented by pyrite, chalcopyrite, sphalerite (with chalcopyrite disease), and minor acanthite and galena (some with inclusions of hessite), Ag-sulfides, and sulfosalts. Dispersed gold occurs as electrum (70 % fineness) associated with chalcopyrite,

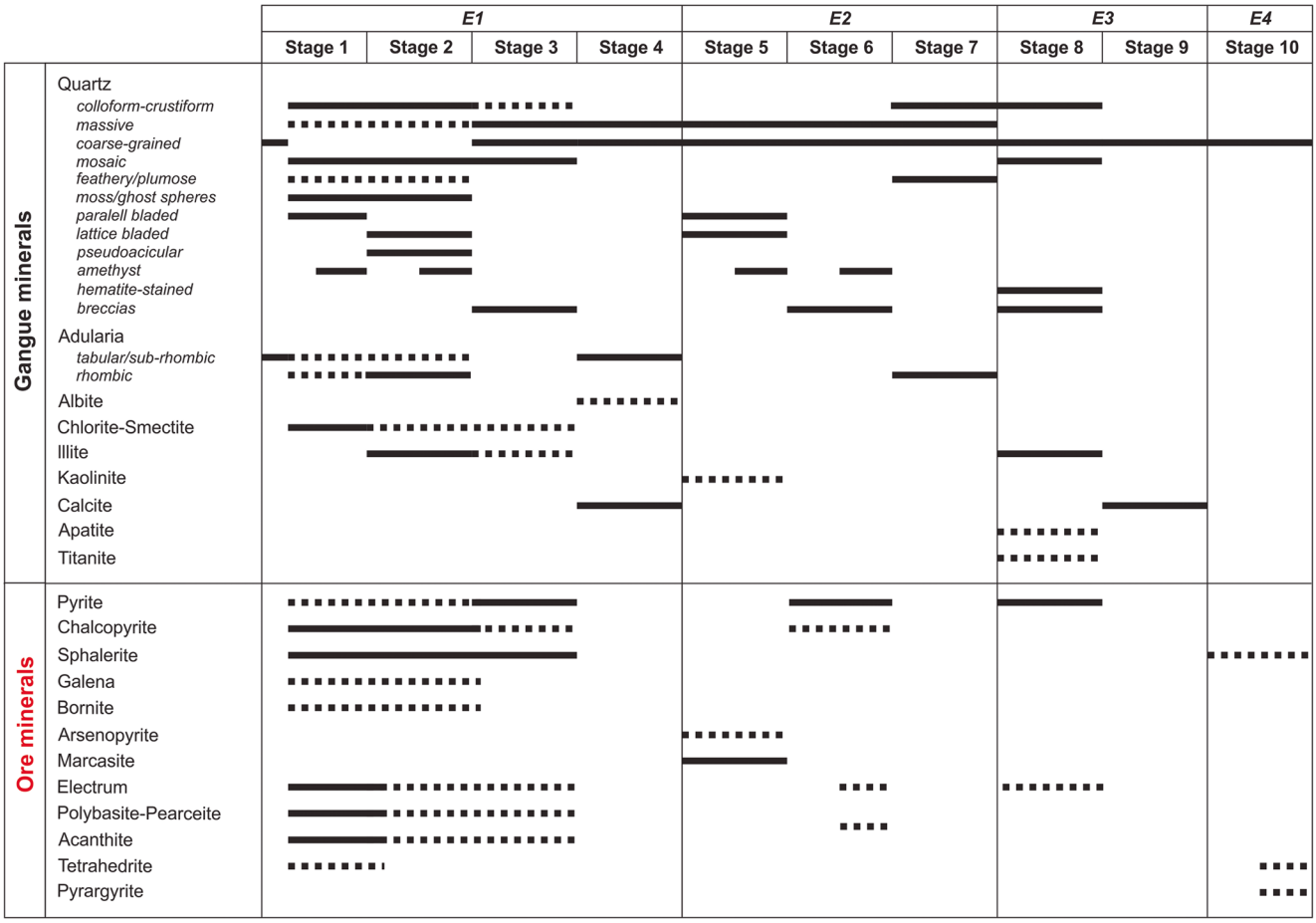

Fig. 5 Paragenetic sequence of ore and gangue minerals, and textural features in the Marianas-San Marcos vein system

and as inclusions in pyrite or intergrown between quartz crystals (Fig. 5; ESM 1).

Stage 3 (S3) is characterized by a brecciated texture with distinct tabular clasts composed of fine-grained colloform-banded chalcedony with abundant sulfides. Clasts are cemented by a fine-grained (mosaic) quartz and with abundant cavities filled with massive to coarse-grained quartz and clay minerals (Figs. 5 and 6d). Ore minerals are dispersed in the matrix, within tabular clasts and as late precipitates filling cavities, and include pyrite with sulfide and minor electrum inclusions, sphalerite, acanthite, polybasite-pearceite, pyrargyrite, and free electrum (Fig. 5).

The last stage 4 (S4) of E1 consists of thin barren veinlets of quartz, adularia, and albite (Figs. 5 and 6e). Tabular to sub-rhombic adularia crystals grow outward from the selvage and are partially overgrown by later albite (Fig. 7f). Toward the center, the adularia crystals are intergrown with coarse-grained quartz and late calcite.

Episode 2

The second episode (E2) consists of three stages and is the most voluminous in all structures (70 to 75 % of the vein volume), and shows lower precious metal contents compared to E1 (Fig. 5).

Stage 5 (S5) consists of quartz showing lattice textures after platy calcite, with cavities filled with late amethyst, marcasite, arsenopyrite, and minor kaolinite (Figs. 5 and 6f). Stage 6 (S6) is a breccia composed of angular to sub-angular clasts of earlier vein fill, and a coarse-grained to massive quartz and late amethyst matrix (Fig. 6g). Ore minerals consist of coarse-grained pyrite containing acanthite, sphalerite, and some electrum inclusions, and chalcopyrite (Fig. 5). Finally, stage 7 (S7) has a broad distribution, and is characterized by veins and veinlets filled by fine-grained rhombic adularia followed by colloform chalcedony banding (with feathery and plumose textures), coarse-grained quartz, and late amethyst (Figs. 5 and 6h).

Episode 3

The third episode (E3) is represented by two stages with low Au–Ag contents. Stage 8 (S8) is typically represented in the northern veins (Mariana Norte and San Marcos), and is characterized by quartz showing colloform-crustiform banding and breccias composed of fine-grained, hematite-stained

quartz (after chalcedony and amethyst), with illite, and minor apatite and titanite (Figs. 5 and 6i). Ore minerals are disseminated in the quartz bands, and associated with massive pyrite (with electrum inclusions), sphalerite, and minor marcasite (Fig. 5). Stage 9 (S9) is characterized by widely distributed barren veinlets, veins, and breccias that are infilled and cemented by coarsely crystalline, rhombic calcite, with some quartz and amethyst (Figs. 5 and 6j).

Episode 4

The fourth episode (E4) is restricted to NNW and E–W trending structures and includes the last stage (S10) that contributes to some high Ag grades. Stage 10 consists of discontinuous bodies of matrix- to clast-supported breccias infilled with chalcedony, illite ± chlorite, iron oxide, and minor apatite in the matrix (Figs. 5 and 6k). Breccia bodies are confined to the vein structure and appear to originate from fault movement. Clasts are derived from earlier vein fillings, and have a diverse range of size and shape. The breccia bodies locally display millimeter-scale deformation bands with cataclastic textures whereby clast size diminishes progressively (Fig. 7g) Ore minerals are common when breccia bodies intercept high-grade intervals of the veins, and include mostly brecciated pyrite crystals with late Ag-tetrahedrite (reaching up to 35 wt% Ag contents, ESM 1) and pyrargyrite (Figs. 5 and 7h). The silver content of S10 suggests partial remobilization of previously deposited metals, mostly due to re-brecciation followed by partial dissolution and Ag-sulfosalt precipitation (e.g., Marshall and Gilligan 1987; Hobbs 1987).

Age of mineralization

Six adularia-rich vein samples from the Marianas-San Marcos vein system were analyzed by $^{40}Ar/^{39}Ar$ geochronology (Fig. 8; ESM 3). All adularias are from the main mineralization (E1) episode. For all analyses of all samples, the mean ages (determined by total fusion of single crystals) are indistinguishable from the plateau ages, and the discussion will focus on the plateau ages. Three samples from Mariana Central were analyzed: sample #102017, sample #91590, and sample #98048 yielded plateau ages of 155.37 ± 0.65 Ma, 154.41 ± 0.43 Ma, and 155.74 ± 0.59 Ma, respectively (Fig. 8). Two samples from the Mariana Norte vein were analyzed and resulted in one plateau age of 156.21 ± 0.45 Ma for the sample #100932, and a slightly younger plateau age of 155.11 ± 0.44 Ma for sample #96335. Sample #111082 was obtained from the San Marcos vein, and although it is characterized by relatively low radiogenic yields and some extraneous, non-atmospheric argon (see ESM 3), it yielded a plateau age of 155.81 ± 0.92 Ma.

The adularia $^{40}Ar/^{39}Ar$ ages from the six samples representing the main mineralizing episode of the Marianas-San Marcos vein system yielded consistent mean ages and plateau ages close to 155 Ma. Samples with coarser grain size (e.g., #100932, with a mean age of 155.27 ± 0.89 Ma) yield approximately the same result as finer-grained samples (e.g., #102017, with a mean age of 155.12 ± 0.71 Ma). A small amount of radiogenic argon loss is indicated by younger ages for the first 5–10 % of release for some samples (the spectra for #91590, #96335, and #95048). For samples with such loss, the plateau age is likely closer to the timing of crystallization than the fusion ages.

All of the results are remarkably consistent, from the standpoint of comparing different samples and results for adularia of a given sample. The most robust results are for sample #102017, which yields a mean age of 155.12 ± 0.71 Ma and a plateau age of 155.37 ± 0.65 Ma for 100 % of the spectrum. This result agrees favorably with the average of mean fusion ages for all six samples, which is 154.92 ± 0.72 Ma (with a MSWD = 1.4), and this mean age is taken as a preferred result for the timing of adularia crystallization in all six samples.

Collectively, the results for this study indicate that the adularia of these six samples formed at 154.92 ± 0.72 Ma, at a temperature that was sufficiently low to permit near-complete retention of radiogenic ^{40}Ar, and have remained below temperatures that could promote substantial argon diffusion in the adularia since that time. The adularia $^{40}Ar/^{39}Ar$ dating constrains the Au–Ag mineralizing hydrothermal activity to this brief Upper Jurassic event.

Hydrothermal alteration

Hydrothermal alteration mineral associations were determined based on short-wave infrared (SWIR) analysis by Goldcorp Inc. along three cross-sections from the Mariana Central, Mariana Norte, and San Marcos vein deposits, with 1- to 3-m interval near the vein, and 5- to 20-m interval into host rock zones (internal report). As Mariana Central 150E was the cross section with higher density of SWIR analyses (Fig. 9), we confirmed and complemented the section with X-ray diffraction (XRD) analysis and petrography, in order to have the

Fig. 6 Photographs of the different mineralization stages from the Marianas-San Marcos vein system. **a** Stage 1, breccia texture composed of chalcedony + chlorite-smectite + sulfide clasts rimmed by coarse, cream colored adularia and crustiform-colloform quartz bands. **b** Stage 2, cockade texture of fine-grained quartz-adularia colloform banding with fibrous-radiating textures around stage 1 fragments. **c** Stage 2, detail of colloform banding with fibro-radiating textures. **d** Stage 3, brecciated texture with distinct tabular clasts of fine-grained colloform-banded chalcedony with abundant sulfides. **e** Stage 4, quartz-adularia-albite veinlets. **f** Stage 5, quartz with lattice texture after platy calcite. **g** Stage 6, quartz matrix crackle breccia with stage 2 clasts. **h** Stage 7, colloform-banded veinlet with fine-grained adularia and amethyst toward the center. **i** Stage 8, chalcedony-hematite-pyrite fluidized breccia. **j** Stage 9, late massive calcite breccia. **k** Stage 10, dark sulfide and silver-rich matrix breccia

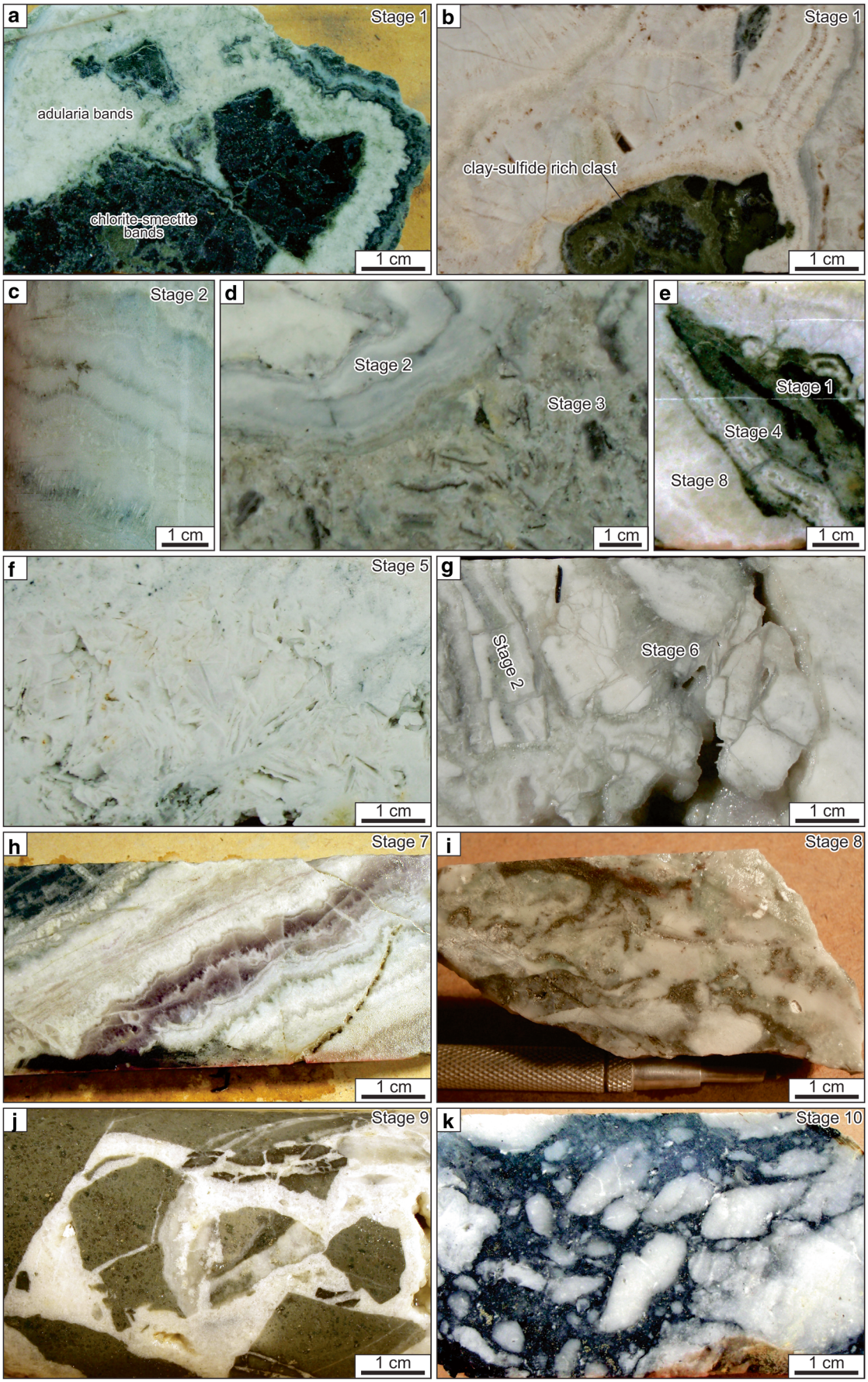
a
Stage 1
adularia bands
chlorite-smectite bands
1 cm
b
Stage 1
clay-sulfide rich clast
1 cm
c
Stage 2
1 cm
d
Stage 2
Stage 3
1 cm
e
Stage 1
Stage 4
Stage 8
1 cm
f
Stage 5
1 cm
g
Stage 2
Stage 6
1 cm
h
Stage 7
1 cm
i
Stage 8
1 cm
j
Stage 9
1 cm
k
Stage 10
1 cm

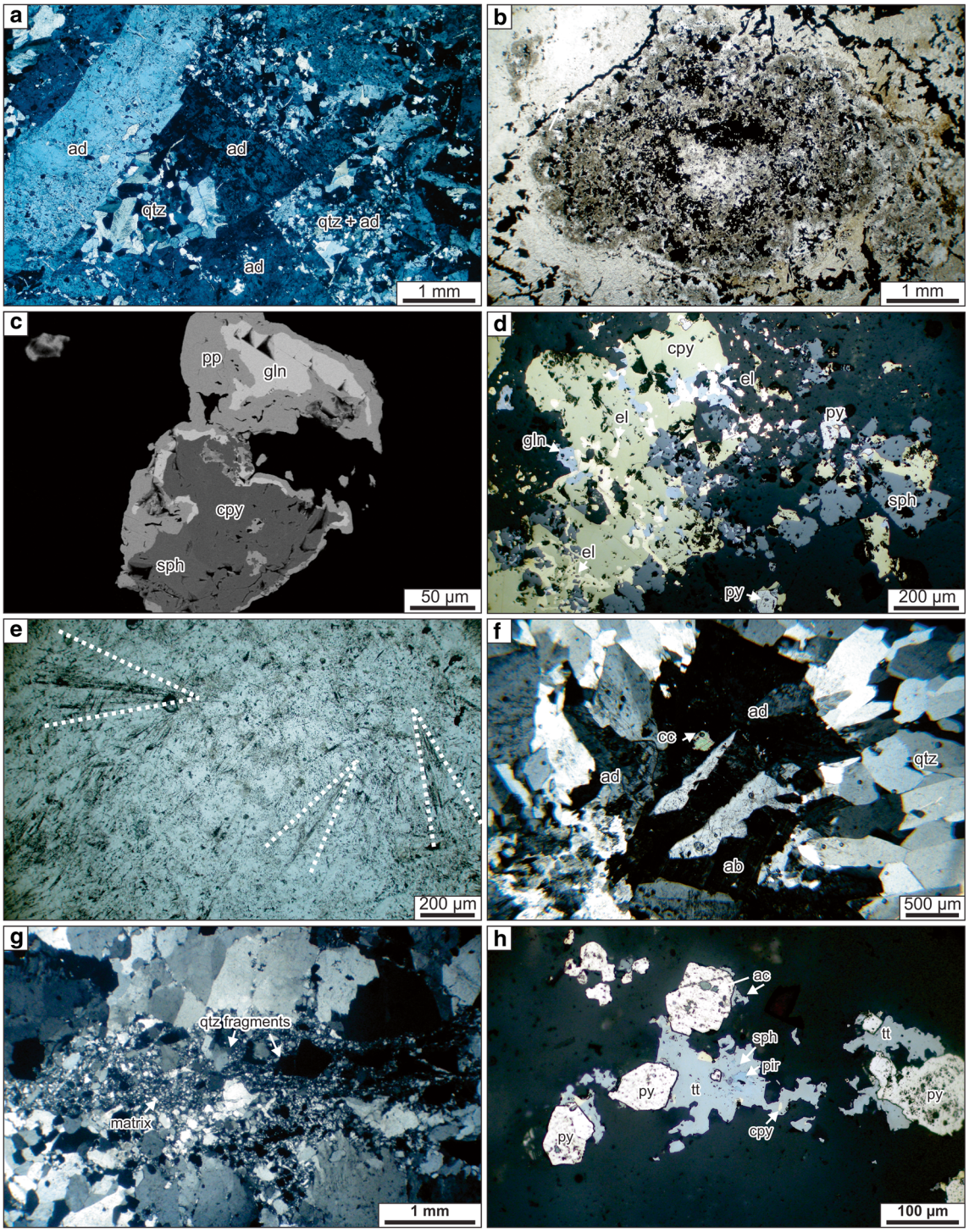

Fig. 7 Microphotographs of the different mineralization stages from the Marianas-San Marcos vein system. **a** Stage 1, early coarse-grained tabular adularia crystals intergrown with quartz and rhombic adularia. **b** Stage 1, quartz recrystallization texture after amorphous silica with associated sulfides. **c** Stage 1, SEM-EDX scan showing concentric aggregates of chalcopyrite and sphalerite followed by galena and overgrown by polybasite-pearceite. **d** Stage 1, massive chalcopyrite with electrum, associated with pyrite, sphalerite, and galena. **e** Stage 2, quartz replacement after radial fibrous minerals. **f** Stage 4, coarse quartz, adularia, and albite veinlets. **g** Stage 10, detail of a deformation band with cataclastic texture consisting of milled quartz fragments. **h** Stage 10, late Ag-sulfosalts with chalcopyrite and sphalerite inclusions occupying vugs. *ab* albite, *ad* adularia, *cc* calcite, *qtz* quartz, *ac* acanthite, *cpy* chalcopyrite, *el* electrum, *gln* galena, *pp* polybasite-pearceite, *pir* pyrargyrite, *py* pyrite, *sph* sphalerite, and *tt* tetrahedrite

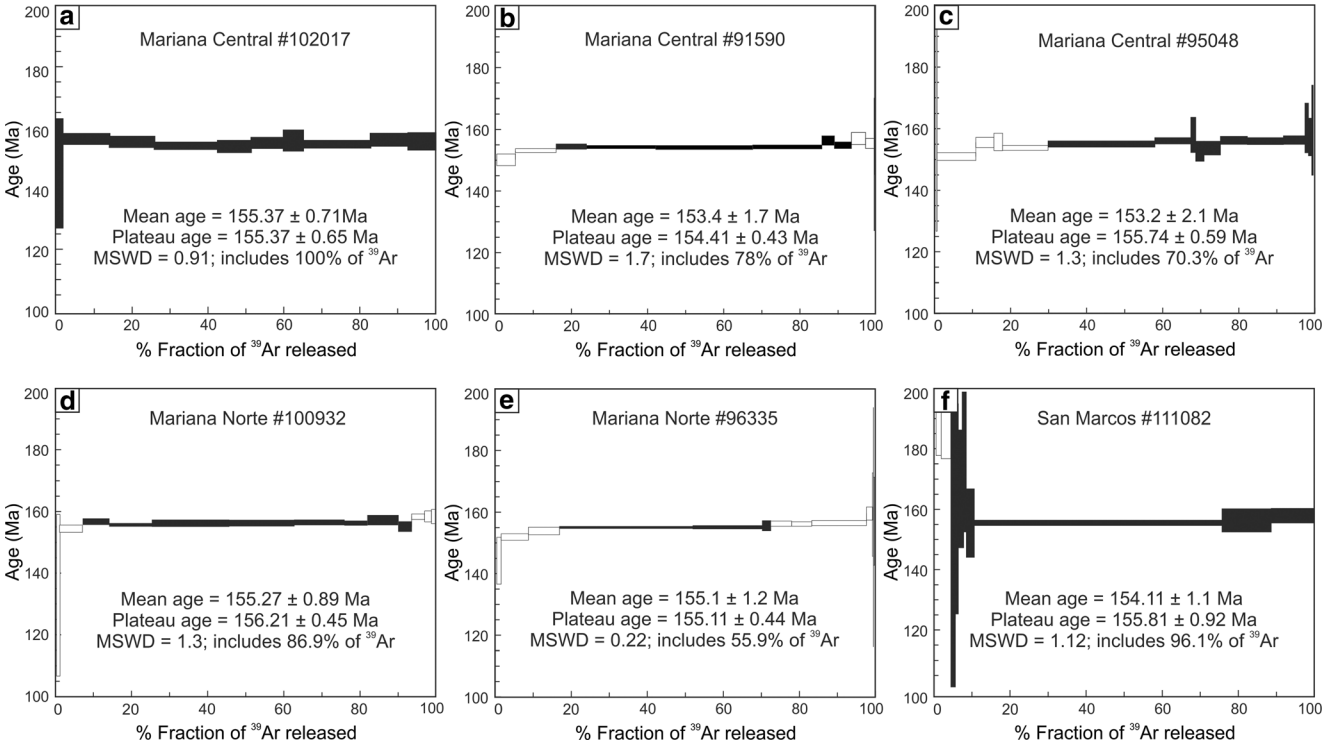

Fig. 8 Summary of $^{40}Ar/^{39}Ar$ data from this study, with mean ages (determined by fusing single crystals) and incremental heating spectra with plateau ages, for the six adularia samples from the Marianas-San Marcos veins. **a**–**c** Mariana Central samples #102017, #91590, and #95048. **d**, **e** Mariana Norte samples #100932 and #96335. **f** San Marcos vein sample #111082. All error estimates are 2σ and error boxes are 1σ. See ESM 3 for further details of the $^{40}Ar/^{39}Ar$ analytical data

complete alteration scheme for these veins, their relationship to ore, and the surrounding geology (Fig. 9; ESM 2).

Alteration immediately adjacent to the vein (up to tens of meters) is dominated by illite ± silica, with high adularia contents ± chlorite ± epidote. This alteration zone is characterized by silicified zones in which primary volcanic textures are obliterated; plagioclase and groundmass are completely replaced by illite patches, and aggregates of quartz and adularia are present. Chlorite replaces mafic minerals and part of the matrix, with minor epidote (found at the footwall of Mariana Central vein, Fig. 9). This intense alteration zone grades laterally into less altered rock where silicification is commonly weak, and primary volcanic textures are normally preserved. Illite content decreases as interstratified illite-smectite increases away from the vein. The outermost zone shows widespread chloritic alteration developed in the andesitic host rock, and primary volcanic textures are completely preserved. In this zone, plagioclase phenocrysts are partially replaced by chlorite, carbonate, and opaque minerals, and pyroxene phenocrysts are commonly replaced by chlorite, calcite, and pyrite.

The shallower part (≤100 m deep from the present surface) of the vein is dominated by a smectite ± chlorite assemblage, affecting the post-mineralization breccia deposits. The base of the post-mineralization breccia is characterized by subhorizontal zones with coarsely crystalline kaolinite, abundant pyrite, opal, and traces of dickite and alunite (Fig. 9). This mineral association is commonly interpreted to be a product of acid alteration (e.g., Hedenquist et al. 2000).

Pyrite is common as a disseminated phase (usually between 5 and 7 vol%), and is typically coarse-grained and observed in all three alteration halos around the vein, but concentrated in the shallower acidic alteration.

Fluid inclusion studies

Most of the mineralization stages in the Marianas-San Marcos vein system contain recrystallized quartz that originally precipitated as amorphous silica and/or chalcedony, and therefore do not record original conditions of formation (e.g., Bodnar et al. 1985; Dong et al. 1995; Sander and Black 1988). Thus, this study focused on defined fluid inclusion assemblages (FIAs) that record original trapping conditions in primary, unmodified inclusions in crystals of quartz, adularia, albite, and calcite, and in secondary and pseudosecondary inclusions trapped along healed fractures that record the conditions of later fracture-healing events (following Bodnar et al. 1985 and Moncada et al. 2012).

The majority of the Marianas-San Marcos vein inclusions are secondary or pseudosecondary in origin and occur along healed fractures in crystals. However, detailed petrography identified some primary inclusions preserved in crystal growth

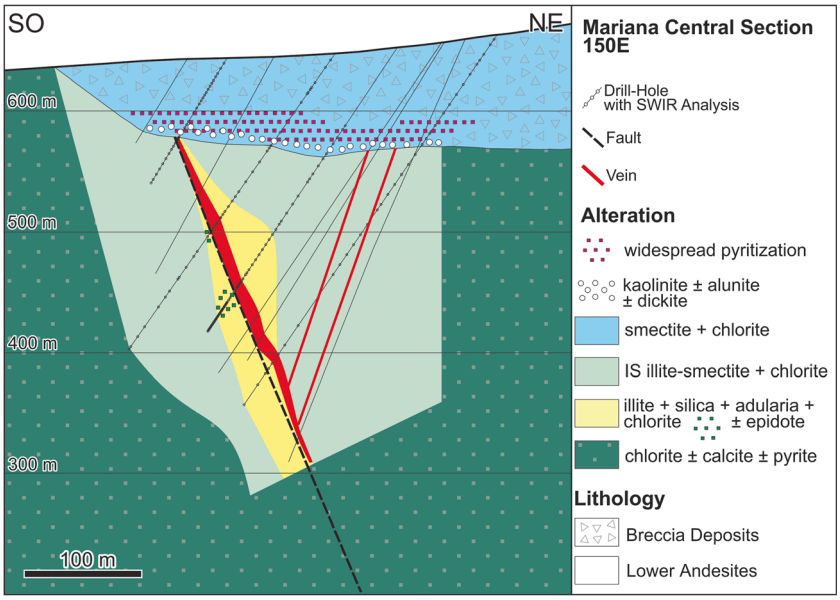

Fig. 9 Representative hydrothermal alteration cross-sections showing the distribution of alteration zones interpreted from SWIR, X-ray, and petrographic analysis of the Mariana Central vein

rims at the base of some quartz crystals, and isolated inclusions in adularia and albite were also interpreted as primary inclusions. Fluid inclusions ranged from 10 to 30 μm in size, and were typically equant in adularia and albite crystals, and irregular or ovoid in quartz. Calcite contains numerous inclusions mirroring the basal pinacoidal morphology, i.e., negative-crystal shapes.

Based on detailed petrographic examination of the different stages of the main mineralizing episode 1 in the Marianas-San Marcos veins, three main fluid inclusion types were identified (Fig. 10a–c): (a) two-phase liquid-rich inclusions with consistent phase ratios (L:V 90 to 95 %), some with trapped illite crystals; (b) two-phase vapor-rich inclusions; and (c) single-phase vapor-filled inclusions without a visible liquid phase.

Thirty-eight liquid-rich FIAs from different stages of the main mineralization episode 1 were selected for microthermometric analysis. Results are displayed in Table 3 and Fig. 10d. The homogenization temperatures (T_h) from measured inclusions range from 302 to 221 °C with salinities of up to 3 % NaCl equiv., but most inclusions homogenize at about 290 to 240 °C and have salinities of 0 to 2 % NaCl equiv. Within individual FIAs, the range in homogenization temperature was typically a few to about 10 °C, with ice-melting temperatures varying by less than a few tenths of a degree Celsius.

Primary inclusions from early adularia crystals from stage 1 yield a T_h range of 286 to 221 °C, with salinities ≤2.9 wt% NaCl equiv., while primary fluid inclusions from coarse-grained quartz coexisting with adularia display T_h from 290 to 263 °C and salinities of 1.7 wt% NaCl equiv. Results from secondary liquid-rich inclusions in quartz show T_h from 261 to 302 °C and salinities up to 1.7 wt% NaCl equiv., overlapping results for primary type FI. Some FIAs show secondary two-phase (liquid-rich and vapor-rich) inclusion trails with measured T_h from 302 to 264 °C and salinities up to 1.7 wt% NaCl equiv. Also, this type of FIA was observed in stage 2 and yielded a T_h of 270 °C and salinities of 1.2 % NaCl equiv. In stage 4, primary inclusions hosted in albite homogenized at 294 to 279 °C and have salinities up to 3 wt% NaCl equiv. Four FIAs show the coexistence of two-phase liquid- and vapor-rich inclusions and single-phase vapor (LV ± V, Table 3). Such inclusions are common in high-grade Au–Ag deposits and have been interpreted to record trapping under intense boiling and/or flashing conditions (Bodnar et al. 1985; Simmons et al. 2005; Moncada et al. 2012).

Episode 1 fluid inclusion data show a negative correlation from higher temperatures and lower salinities to lower temperatures and higher salinities. This pattern suggests cooling and mixing between a higher salinity and lower temperature brine, and a lower salinity and higher temperature fluid.

Three primary, liquid-rich inclusions were measured in late rhombic calcite from stage 9, within the low-grade to barren episode 3. These inclusions show T_h of 290 to 240 °C, and salinities close to 1 wt% NaCl equiv., overlapping the episode 1 fluid temperature and salinities.

The dominance of NaCl in the fluids is suggested by eutectic melting temperatures (T_e) that are close to −22 °C (Bodnar 2003). Vapor-rich inclusions were analyzed by Raman spectroscopy and CO_2 peaks were not observed. Based on Hedenquist and Henley (1985a), ice-melting temperatures in the range of 0 to −1.5 °C correspond to CO_2

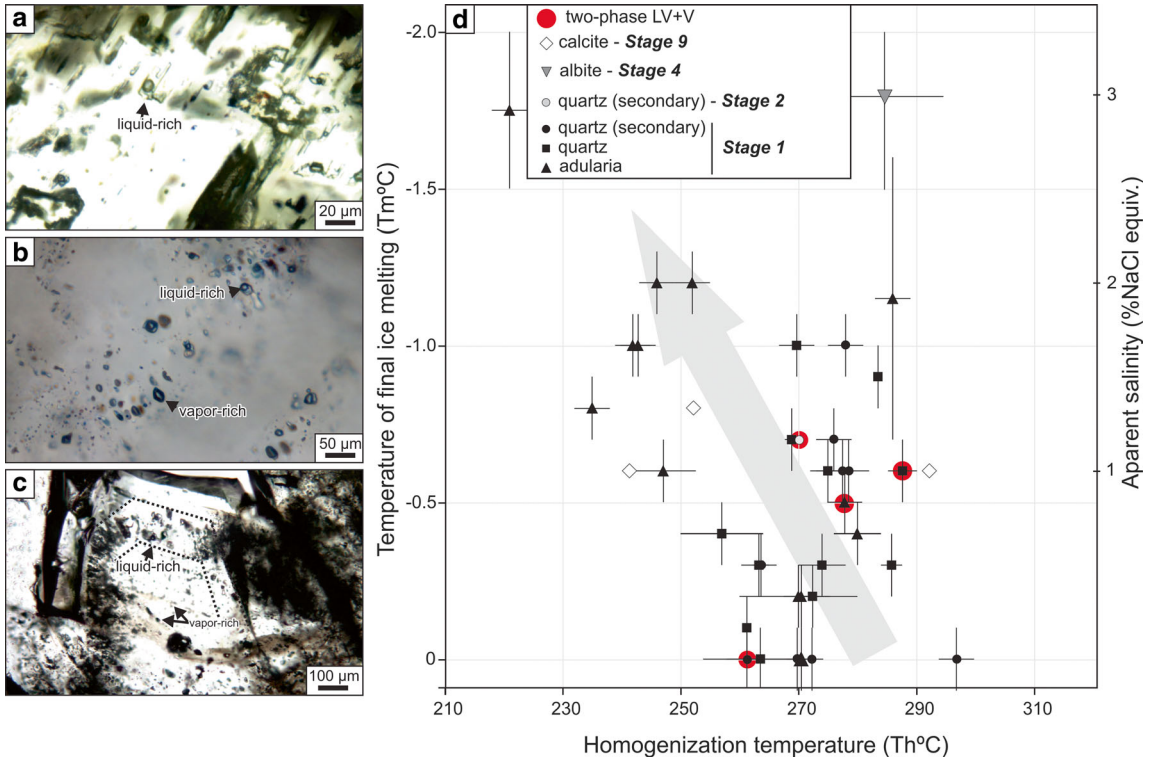

Fig. 10 **a** Rectangular-shaped primary liquid-rich inclusions in an adularia crystal. **b** Secondary, vapor-rich fluid inclusion trail crosscutting euhedral quartz crystal of early stage 1. **c** Detail of secondary coexisting vapor-rich and liquid-rich inclusions in early quartz of stage 1. **d** Average homogenization temperature versus average ice-melting temperature for described fluid inclusion assemblages (FIAs) from the Marianas-San Marcos vein system. Each FIA consists of two or more fluid inclusions with consistent microthermometric behavior. *Horizontal/vertical bars* are the ranges of T_m and T_h values from Table 3. Salinities are given in NaCl wt% equiv. using T_m values and the salinity-freezing point depression table from Bodnar and Vityk (1994)

contents less than 3.7 wt%. LA-ICP-MS analysis of fluid inclusions in quartz from the episode 1 detected Pb and Zn, and higher concentrations of Na (655 to 8287 ppm), K (854 to 9821 ppm), As (28 to 357 ppm), and Sb (74 to 980 ppm). These concentrations are different from those of the episode 3 calcite (see Table 4), although the latter has higher Ca (8596 to 8644 ppm), and may record a different type of fluid for these events.

Regarding the wide ranges of T_h which are typically registered in epithermal deposits (e.g., Faure et al. 2002; Moncada and Bodnar 2012; Simpson et al. 2015), all measured inclusions overlap in temperature and in calculated salinity, with no systematic variation as a function of paragenetic stages or gangue material (Fig. 10d), suggesting a sustained steady-state hydrothermal system during at least E1, with restricted boiling periods.

The last fluid events are recorded by coexisting secondary liquid- and vapor-rich inclusions that do not record formation conditions of host quartz crystals and are most likely related to a later boiling stage during the vein formation. Assuming hydrostatic conditions, and the boiling point with depth curves from Haas (1971), the veins appear to have formed 600 to 800 m below the former water. Fluid inclusion data indicate that late barren calcite from E3 formed from dilute fluids (1–1.5 wt% NaCl equiv.) between 240 and 290 °C, similar to the temperature range of Au–Ag bearing E1.

Stable isotopes

Oxygen and hydrogen

Representative samples of adularia, paragenetically related clay-rich (chlorite-smectite) bands, and late chlorite-smectite from stage 1 were selected for hydrogen and oxygen isotope analysis in order to characterize the hydrothermal fluids, and to identify the source of water in the system (Table 5).

The $\delta^{18}O$ value from adularia varies from 3 to 6.6‰, early chlorite-smectite $\delta^{18}O$ ranges from 1.4 to 2.7‰ and δD of −79.2 to −70‰, and late chlorite-smectite has higher $\delta^{18}O$ values (ranging from 3.6 to 4.5‰), but similar δD values (−79.8 to −71.3‰).

Assuming an average temperature of 250 °C from the fluid inclusion data, the mineral isotopic data were used to calculate the isotopic composition of fluid that would be in equilibrium with the minerals at 250 °C. The calculated $\delta^{18}O_{water}$ for adularia ranges between −2.8 and 0.8‰ using the fractionation factors from Zheng (1993). For chlorite-smectite, the Sheppard and Gilg (1996) equations were used. For the early

Table 3 Microthermometry results from Marianas-San Marcos vein system

Sample_ chip_ FIA	Drill-Hole	Vein	Stage	Mineral	*n*	Type	T_e (°C)	T_h range (°C)	T_h average (°C)	T_m range (°C)	T_m average (°C)	Salinity (%NaCl eq.)	Observations
102878_2_2	MDD-1060	MC	1	Adularia	>5	p	–	276–284	280.0	−0.5 to −0.3	−0.4	0.71	
102878_2_2	MDD-1060	MC	1	Adularia	2	p	–	270.5	270.5	−0.3 to −0.1	−0.2	0.5	
102878_4_1	MDD-1060	MC	1	Adularia	1	p	–	252	252.0	−1.3 to −1.1	−1.2	2.07	LA-ICP-MS
102878_A_1	MDD-1060	MC	1	Adularia	6	p	–	286	286.0	−1.6 to −0.7	−1.15	1.91	
102878_A_3	MDD-1060	MC	1	Adularia	2	p	–	241.9	241.9	−1.1 to −0.9	−1	1.74	
102878_A_4	MDD-1060	MC	1	Adularia	5	p		246	246.0	−1.3 to −1.1	−1.2	2.07	
112251_1_3	MDD-1104	MC	1	Adularia	3	p	–	268–273	270.5	0	0	0.00	Trapped illite
112251_2_1	MDD-1104	MC	1	Adularia	2	p	–	260–280	270.0	−0.3 to −0.1	−0.2	0.35	
112251_3_1	MDD-1104	MC	1	Adularia	6	p	–	241.6–252.6	247.1	−0.7 to −0.5	−0.6	0.71	
112672#2_2_A	MDD-1119	MC	1	Adularia	5	p	–	274.9–280.8	277.9	−0.6 to −0.4	−0.5	0.88	LV + V
112672_A_2	MDD-1119	MC	1	Adularia	1	p	–	221	221.0	−1.5 to −2	−1.7	2.9	
112672_A_3	MDD-1119	MC	1	Adularia	2	p	–	242.8	242.8	−1.1 to −0.9	−1	1.74	
112672_A_4	MDD-1119	MC	1	Adularia	9	p	–	235	235.0	−0.9 to −0.7	−0.8	1.4	
185452_4	MDD-11294	MC	1	Quartz	>5	p	–	250	250.0	−0.6 to −0.4	−0.5	0.88	
112251_1_1	MDD-1104	MC	1	Quartz	>10	p	–	270–278	274.0	−0.4 to −0.2	−0.3	0.53	Trapped illite
112251_4_2	MDD-1104	MC	1	Quartz	2	s	–	262.3–265	263.6	−0.4 to −0.2	−0.3	0.53	LA-ICP-MS
112251_4_3	MDD-1104	MC	1	Quartz	6	s	–	270.4–274.2	272.3	0	0	0	Trapped illite; LA-ICP-MS
112672#2_1_A	MDD-1119	MC	1	Quartz	>10	s	–	295–310	302.5	−0.2 to 0	−0.1	0.18	
112672#2_1_B	MDD-1119	MC	1	Quartz	5	ps	–	257.8–269.3	263.5	0	0	0	Trapped illite
112672#2_1_C	MDD-1119	MC	1	Quartz	5	ps	–	285.2–290.1	287.6	−0.7 to −0.5	−0.6	1.05	LV + V
112672_1_1	MDD-1119	MC	1	Quartz	6	s	–	273–282	277.5	−0.7 to −0.5	−0.6	1.05	
112672_1_2	MDD-1119	MC	1	Quartz	5	p	–	267.7–270	268.9	−0.8 to −0.6	−0.7	1.23	
112672_1_3	MDD-1119	MC	1	Quartz	3	p	–	263.3	263.3	−0.4 to −0.2	−0.3	0.53	
112672_3_1	MDD-1119	MC	1	Quartz	>10	p	–	250–264	257.0	−0.5 to −0.3	−0.4	0.71	Trapped illite
185452_1_1	MDD-11294	MC	1	Quartz	6	p	–	269.7	269.7	−1.1 to −0.9	−1	1.74	
185452_1_1	MDD-11294	MC	1	Quartz	2	s	–	275–277	276.0	−0.8 to −0.6	−0.7	1.23	
185452_1_2	MDD-11294	MC	1	Quartz	>10	s	–	296.8	296.8	0	0	0	
185452_1_2	MDD-11294	MC	1	Quartz	>10	s	–	277–279	278.0	−1.1 to −0.9	−1	1.74	LA-ICP-MS
185452_1_2	MDD-11294	MC	1	Quartz	2	s	–	278–279	278.5	−0.7 to −0.5	−0.6	1.05	
185452_1_3	MDD-11294	MC	1	Quartz	3	p	−24.3	272.4	272.4	−0.3 to −0.1	−0.2	0.35	LA-ICP-MS
185452_1_4	MDD-11294	MC	1	Quartz	4	s	–	268.9–270.7	269.8	0	0	0	
185452_1_5	MDD-11294	MC	1	Quartz	5	p	–	284–287.6	285.8	−0.4 to −0.2	−0.3	0.53	
185452_2_1	MDD-11294	MC	1	Quartz	6	p	–	275	275.0	−0.7 to −0.5	−0.6	1.05	
222797_1_3	MDD-12155	MC	1	Quartz	>10	p	–	275–292	283.5	−1.0 to −0.8	−0.9	1.57	Trapped illite; LA-ICP-MS
222797_1_4	MDD-12155	MC	1	Quartz	>10	s	–	253.5–269	261.2	−0.2 to 0	−0.1	0.18	LV + V
91886_1_1	MDD-1041	MC	2	Quartz	3	s	−21	270	270.0	−0.8 to −0.6	−0.7	1.23	LV + V
107530_A_1	MDD-1061	MN	4	Albite	3	p	–	278.8–294.6	284.5	−2.1 to −1.6	−1.8	3.06	
112245_1	MDD-1104	MC	9	Rhombic calcite	3	p	–	290–295	292.5	−0.7 to −0.5	−0.6	1.05	
185452_3_1	MDD-11294	MC	9	Rhombic calcite	5	p	−21.5	249–252	251.0	−0.9 to −0.7	−0.8	1.4	LA-ICP-MS
185482_3_2	MDD-11294	MC	9	Rhombic calcite	8	p	–	237.8–241.6	240.0	−0.7 to −0.5	−0.6	1.05	LA-ICP-MS

MC Mariana Central, *MN* Mariana Norte, T_h homogenization temperature, T_m ice-melting temperature, T_e eutectic temperature, *n* number of analyzes, *p* primary, *s* secondary, *ps* pseudosecondary

clays, we used a temperature of 250 °C due to the paragenetic relationship of early clays and adularia, and the results are between −2.6 and −3.9‰ for $\delta^{18}O_{water}$ and −55 to −59.2‰ for δD_{water}. For the late smectite-chlorite, and due to the absence of data on the temperature of formation, a temperature of 120 °C was assumed based on data from similar late clays in the Hishikari deposit in Japan (Matsuhisa and Aoki 1994; Faure et al. 2002). Results indicate a $\delta^{18}O_{water}$ of −7.9 to −8.8‰ and δD_{water} of −56.4 to 64.8‰.

Figure 11 shows the oxygen and hydrogen isotopic composition of Marianas-San Marcos water, compared with reference values from volcanic vapors, felsic magmas and porphyry ores (Hedenquist and Lowenstern 1994; Taylor 1986; Giggenbach 1992), and the $\delta^{18}O$ isotopic values from the Deseado Massif epithermal deposits (Schalamuk et al. 1997;

Table 4 LA-ICP-MS results from the Marianas-San Marcos system

Sample	Drill-Hole	Vein	Stage	Host	type	Na	Mg	K	Ca	Mn	Fe	Cu	Pb	Zn	As	Sb	Se	Ag	Te	Au
112251_4	MDD-1104	MC	1	Quartz	p	8717	–	854	526	–	–	–	3.4	–	27.8	181.4	–	–	–	–
112251_4	MDD-1104	MC	1	Quartz	p	1518	–	9821	820	36.9	–	–	2.4	82.1	29.9	169.9	–	–	–	–
102878_4_1	MDD-1060	MC	1	Quartz	s	1082	–	9122	131	7.9	–	–	–	–	–	28.9	–	–	–	–
112251_4_3	MDD-1104	MC	1	Quartz	s	8287	–	4503	509	–	–	–	–	–	113.5	425.9	–	–	–	–
112251_4_2	MDD-1104	MC	1	Quartz	s	6838	–	3604	1528	–	–	–	2.1	–	–	206.9	–	–	–	–
22297_1_3	MDD-12155	MC	1	Quartz	s	655	–	7428	22	–	46.2	–	1.0	482.8	36.8	73.6	–	–	–	–
22297_1_3	MDD-12155	MC	1	Quartz	s	2464	–	5452	73	–	–	–	1.3	–	33.5	69.3	–	–	–	–
22297_1_3	MDD-12155	MC	1	Quartz	s	4419	–	1555	104	–	–	–	–	–	356.3	979.6	–	–	–	–
185452_1_3	MDD-11294	MC	1	Quartz	s	1767	–	9779	83	–	–	–	5.0	–	78.6	185.8	–	–	–	–
185452_3_2	MDD-11294	MC	9	Calcite	p	54	–	10	8596	44.3	0.7	–	0.0	–	–	–	–	–	–	–
185452_3_3	MDD-11294	MC	9	Calcite	p	6	1.02	1	8644	46.7	0.8	–	–	–	0.2	–	–	–	–	–
185452_3_4	MDD-11294	MC	9	Calcite	p	9	1.76	1	8627	62.5	1.3	–	–	–	0.1	–	–	–	–	–

Values in ppm

MC Mariana Central, *p* primary, *s* secondary

Guido 2002; Moreira 2005), based on δO from quartz. Water associated with adularia and early clay chlorite-smectite bands plots between the meteoric line and volcanic waters, while late clays fall closer to the meteoric water line, suggesting that later fluids are diluted by meteoric water.

Carbon and oxygen

The isotopic composition of late calcite veins from stage 9 (barren episode) ranges from −9.2 to −8.5 ‰ and the equilibrium $\delta^{13}C$ compositions of carbon dioxide for most of these data fall between –7.22 and −7.85 ‰ (Table 5). The $\delta^{18}O$ composition of calcite ranges from −1.2 to 1.2 ‰. Assuming an average 250 °C temperature from fluid inclusions, the calculated $\delta^{18}O$ compositions of water in equilibrium with calcite range from −6.1 to −8.5 ‰, using the fractionation factors from O'Neil et al. (1969) and Friedman and O'Neil (1977). Fluids in equilibrium with late calcite veinlets display a lighter $\delta^{18}O$ composition compared to early adularia and chlorite-smectite bands from stage 1 (−3 to 0 ‰), and are close to the Jurassic meteoric waters and to the late clays (Fig. 11).

Sulfur isotopes

To determine the source of sulfur in ore fluids, the isotopic composition of pyrite formed during stage 1 was determined (Table 5). Results yielded $\delta^{34}S$ values ranging from −0.5 to 0.9 ‰, and the $\delta^{34}S$ calculated for the fluid in equilibrium with pyrite is −0.5 to −1.9 ‰, using the Ohmoto and Rye (1979) formula at 250 °C. The obtained values are consistent with a magmatic sulfur source, similar to other epithermal deposits in the Deseado Massif (Jovic et al. 2011).

Discussion

Origin and evolution of the Marianas-San Marcos vein system

The Marianas-San Marcos veins consist of a complex paragenetic sequence that can be divided into ten stages, and simplified into four episodes: the Au- and Ag-rich episode (E1), the massive banded quartz episode (E2), the waning stage episode (E3), and the late tectonic–hydrothermal episode (E4).

Episode 1 (E1) is the most important economically. It represents a small volume proportion of the total vein material, (<10 % of the vein infill), but contains most of the ore minerals, which precipitated within restricted bands or patches associated with early clays, quartz, and adularia in crustiform-colloform bands from stage 1 and/or disseminated within stage 2 quartz bands. The overall sulfide content and the relative abundance of adularia progressively decrease toward the end of the episode (Fig. 5). Gold occurs as electrum (60–70 % fineness) accompanied by pyrite, chalcopyrite, Fe-poor-sphalerite, Ag-sulfosalts (Se-rich polybasite-pearceite, tetrahedrite-tennantite, pyrargyrite), and minor galena (ESM 1). This sulfide association is more typical of an intermediate sulfidation state system (Hedenquist et al. 2000; Einaudi et al. 2003; Sillitoe and Hedenquist 2003; Simmons et al. 2005). $^{40}Ar/^{39}Ar$ ages on E1 adularia from the three studied veins (Mariana Central, Mariana Norte, and San Marcos) yield a collective mean age of 154.92 ± 0.72 Ma. Fluid inclusions homogenized at 290 to 230 °C clustered at 270 °C, and show salinities of less than 3 % NaCl equiv. (generally below 2 %). Proximal hydrothermal alteration comprises quartz, adularia, illite, illite/smectite, and smectite, indicating near-neutral fluid pH conditions at temperatures ranging from 220 to 150 °C (Simmons and Browne 2000), but the occurrence of local epidote suggests a relatively

Table 5 Oxygen, carbon, and sulfur isotope data from the Marianas-San Marcos vein system

Sample	Drill-Hole	Vein	Deep (m)	Stage	Host	Description	$\delta^{18}O$ (‰, VSMOW)	δD (‰, VSMOW)	$\delta^{18}O_{water}$ (‰, VSMOW)	δD_{water} (‰, VSMOW)	$\delta^{13}C$ (‰, VPDB)	$\delta^{13}C_{fluid}$ (‰, VPDB)	$\delta^{34}S$ (‰, VCDT)	$\delta^{34}S_{fluid}$ (‰, VCDT)
96336	MDD-1015	MN	509	1	Adularia	Coarse tabular adularia	5.4		−0.4[a]					
112251	MDD-1104	MC	364	1	Adularia	Coarse tabular adularia	3.0		−2.8[a]					
112672	MDD-1119	MC	420	1	Adularia	Fine rhombic adularia	5.1		−0.7[a]					
106980	SDD-1048	SM	330	1	Adularia	Fine rhombic adularia	6.6		0.8[a]					
102059	MDD-1028	MC	467	1	Adularia	Coarse tabular adularia	4.7		−1.1[a]					
102059	MDD-1028	MC	467	1	Chlorite-smectite	Early	1.4	−79.2	−3.9[b]	−59.2				
96336	MDD-1015	MN	509	1	Chlorite-smectite	Early	2.7	−72.0	−2.6[b]	−57.0				
112251	MDD-1104	MC	364	1	Chlorite-smectite	Early	2.1	−70.0	−3.2[b]	−55.0				
107532	MDD-1061	MN	469	1	Chlorite-smectite	Late	3.6	−71.3	−8.8[b]	−56.4				
79341	SDD-1013	SM	474	1	Chlorite-smectite	Late	4.5	−79.8	−7.9[b]	−64.8				
102059	MDD-1028	MC	467	9	Calcite	Late veins	0.6		−6.7[c]		−8.5	−7.22[c]		
100926	MDD-1032	MN	520	9	Calcite	Late veins	1.2		−6.1[c]		−9.0	−7.72[c]		
107532	MDD-1061	MN	469	9	Calcite	Late veins	−1.2		−8.5[c]		−9.2	−7.85[c]		
112224	MDD-1104	MC	482	9	Calcite	Late veins	−1.2		−8.5[c]		−8.7	−7.35[c]		
112245	MDD-1104	MC	370	9	Calcite	Late veins	1.0		−6.3[c]		−8.7	−7.38[c]		
112672	MDD-1119	MC	420	1	Pyrite	Sulfide-rich bands							0.2	−1.2[d]
107532	MDD-1061	MN	469	1	Pyrite	Sulfide-rich bands							0.9	−0.5[d]
106980	SDD-1048	SM	330	1	Pyrite	Sulfide-rich bands							−0.5	−1.9[d]

MC Mariana Central, *MN* Mariana Norte, *SM* San Marcos

[a] Calculated using Zheng (1993) fractionation equation at 250 °C

[b] Calculated using Sheppard and Gilg (1996) fractionation at 250 °C for early clays and 120° for late clays

[c] Calculated using fractionation equation of O'Neil et al. (1969) and Friedman and O'Neil (1977) at 250 °C

[d] Calculated using fractionation equation of Ohmoto and Rye (1979) at 250 °C

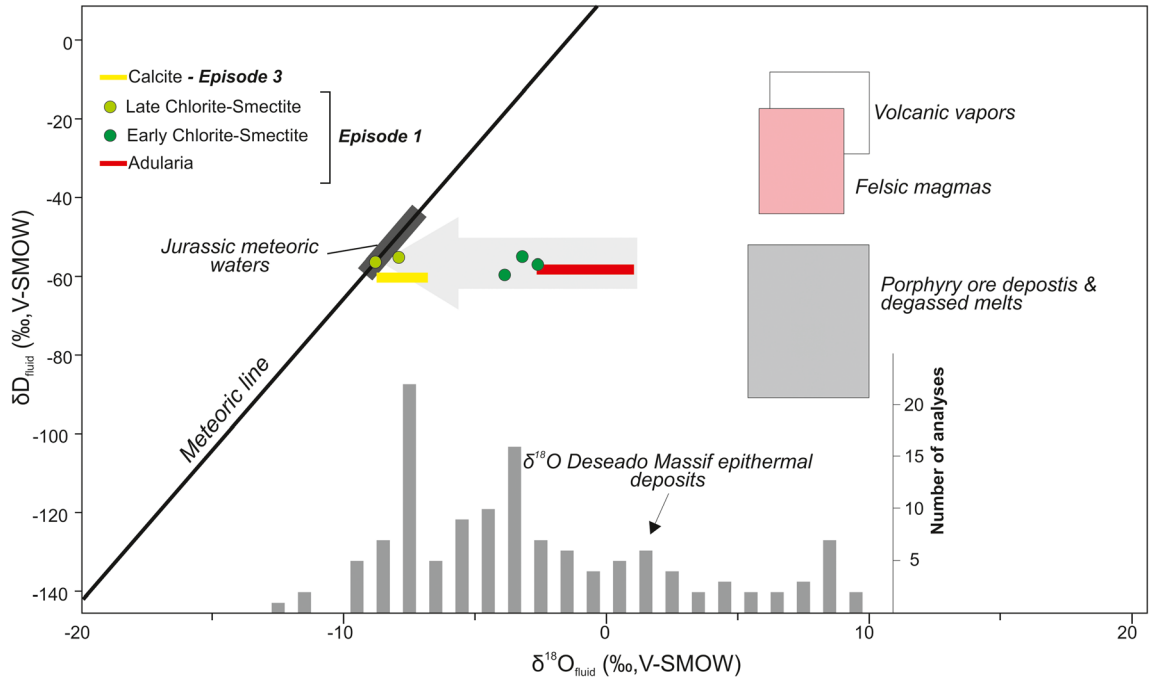

Fig. 11 Stable isotope (δD versus $\delta^{18}O$) plot showing the isotopic ratios of Jurassic meteoric waters for the Deseado Massif (Cravero et al. 1991), volcanic vapors, felsic magmas, and porphyry ores (Hedenquist and Lowenstern 1994; Taylor 1986; Giggenbach 1992), compared to calculated waters in equilibrium with adularia and clay minerals of stage 1, and calcite from stage 9, of the Marianas-San Marcos vein system. Histograms of isotopic values from the Deseado Massif epithermal deposits (Schalamuk et al. 1997; Guido 2002; Moreira 2005)

higher (>240 °C) hydrothermal fluid temperature (Browne et al. 1989; Hedenquist et al. 1996). Oxygen and Deuterium stable isotopes indicate mixing of Jurassic magmatic and meteoric waters (see Cravero et al. 1991), in agreement with convection of meteoric waters through the volcanic pile and a consequent oxygen shift due to isotopic exchange (e.g., Taylor 1986). Consistent hydrogen isotope values have also been noted in active geothermal systems during water/rock interaction (e.g., Sawkins et al. 1979; Giggenbach 1992). Sulfur stable isotopic results are consistent with derivation of the sulfur from a magmatic source, similar to most epithermal ore deposits in the Deseado Massif (e.g., Jovic et al. 2011). The presence of ore-bearing, colloform-banded textures with amorphous silica, platy calcite replaced by quartz, adularia, and coexisting liquid-rich and vapor-rich fluid inclusions suggest boiling (and locally flashing) as the principal mechanism for precious metals deposition for this episode (e.g., Bodnar et al. 1985; Brown 1986; Simmons and Christenson 1994; Corbett and Leach 1997; Hedenquist et al. 2000; Simmons et al. 2005). The presence of quartz replacement textures after possible zeolites also reflects fluctuations in aqueous CO_2 content due to boiling (e.g., Browne and Ellis 1970; Simpson and Mauk 2011), but the negative correlation of temperature versus salinity of the FIAs from episode 1 (Fig. 10) suggests that cooling and mixing processes were also involved in metal precipitation.

Episode 2 (E2) and episode 3 (E3) are volumetrically important, occupying up to 80 % of the vein infill, but adding only small amounts of metal to the vein system. During these episodes, the structures were filled successively by quartz (E2 and E3) and late calcite (E3) stages (Fig. 5), with massive, brecciated, and chalcedony colloform banding textures. Although some boiling evidence is observed in E2 episode (platy calcite in stage 5 and adularia in stage 7), they are not related to metal deposition. Ore mineralogy of these episodes comprises pyrite, arsenopyrite, and marcasite with scarce electrum (Fig. 5), likely associated with a low sulfidation state of the fluid (Hedenquist et al. 2000; Einaudi et al. 2003; Sillitoe and Hedenquist 2003; Simmons et al. 2005). During episode 3, development of the widely distributed quartz-amethyst veinlets and hematite-staining of stage 8 suggests a diluted, oxygenated groundwater with higher meteoric water input (e.g., Brathwaite and Faure 2002; Vaughan and Craig 1997), and the calcite veins of stage 9 are interpreted as the collapse of CO_2 steam-heated waters during the waning stages of hydrothermal activity (e.g., Simmons et al. 2000).

The last episode (E4) is interpreted to be a late-stage tectonic–hydrothermal event (stage 10, Fig. 5), evidenced by local tectonic reactivation characterized by cohesive fault breccia (Passchier and Trouw 2005). Breccia bodies are matrix-supported, have angular-shaped vein clasts with cataclastic textures, and are cemented by recrystallized quartz after chalcedony. Ore minerals in the breccia are characterized by crackle pyrite crystals and undeformed silver sulfosalts, which are interpreted to have crystallized during this stage (Ag-rich tetrahedrite and pyrargyrite in veinlets and filling cavities, Fig. 5). Normally, where the late tectonic–

hydrothermal breccia crosscuts high-grade portions of the veins, the breccia register higher Ag values, suggesting mechanical and chemical remobilization of the silver (e.g., Gilligan and Marshall 1987; Marshall and Gilligan 1987; Hobbs 1987; Gu et al. 2007; Páez et al. 2016).

Reconstruction of the volcanic and hydrothermal systems

The Jurassic volcanic sequence at Cerro Negro evolved through two main events defining variations in volcanic style, composition, and age. The Lower Section overlies a non-outcropping metamorphic basement, and can reach several hundreds of meters of andesitic-dacitic lava flows and pyroclastic units older than 159 Ma, the age defined by Lopez (2006) for the Medium Andesites (Fig. 2; ESM 4). The sequence is intruded by dacitic to andesitic subvolcanic porphyries that were dated by Lopez (2006) at 157 and 156 Ma, respectively. The Lower Section can be interpreted as a product of a long-lasting (>3 Ma) polygenetic volcanic edifice (Cas and Wright 1988; Sigurdsson et al. 2015) of intermediate composition that started with lava flows and pyroclastic deposits and ended with shallow intrusions.

During the last stages of andesitic-dacitic volcanism, a hydrothermal system was active, producing the Marianas-San Marcos epithermal veins and related hydrothermal alteration within NW and EW striking half-graben structures. $^{40}Ar/^{39}Ar$ ages on adularia from the initial episode yielded an average age of 154.92 ± 0.72 Ma, constraining the hydrothermal event to approximately 1 Ma after the andesitic subvolcanic intrusion, and in agreement with the 156.6 to 151.2 Ma range reported from Ar-Ar ages in vein adularia from different epithermal deposits from the western Deseado Massif (Table 1).

Afterwards, a district-scale discordance is represented by post-epithermal deposits recorded at Cerro Negro by breccia aprons, acidic volcaniclastic deposits (Shatwell et al. 2011), and lava domes of the Upper Section. Based on field relationships, the Upper Section rhyolitic sequence is younger than the 155 Ma epithermal mineralization, in agreement with reported ages for similar rocks in the northwestern Deseado Massif (154.6 to 147.6 Ma from San José and Río Pinturas localities, Table 1). At this stratigraphic level, a large (>15 km^2) Jurassic geothermal system, with hot spring and hydrothermal eruption breccia deposits, was preserved (Lopez 2006; Guido and Campbell 2012) in proximity of the Marianas-San Marcos vein system (Fig. 2). These deposits were precipitated in a fluvio-lacustrine environment, hosted in the Tuff and Tuffites unit, but genetically and spatially linked to the rhyolitic domes according to Guido and Campbell (2012). In such a geothermal setting, the breccia aprons above mineralized veins could be products of hydrothermal eruptions, as was interpreted by Permuy Vidal et al. (2013), or could reflect transport and deposition of near-by hot spring centers with related eruption breccias. Similar breccias were described by Hedenquist and Henley (1985b), Nelson and Giles (1985), Browne and Lawless (2001), Christiansen et

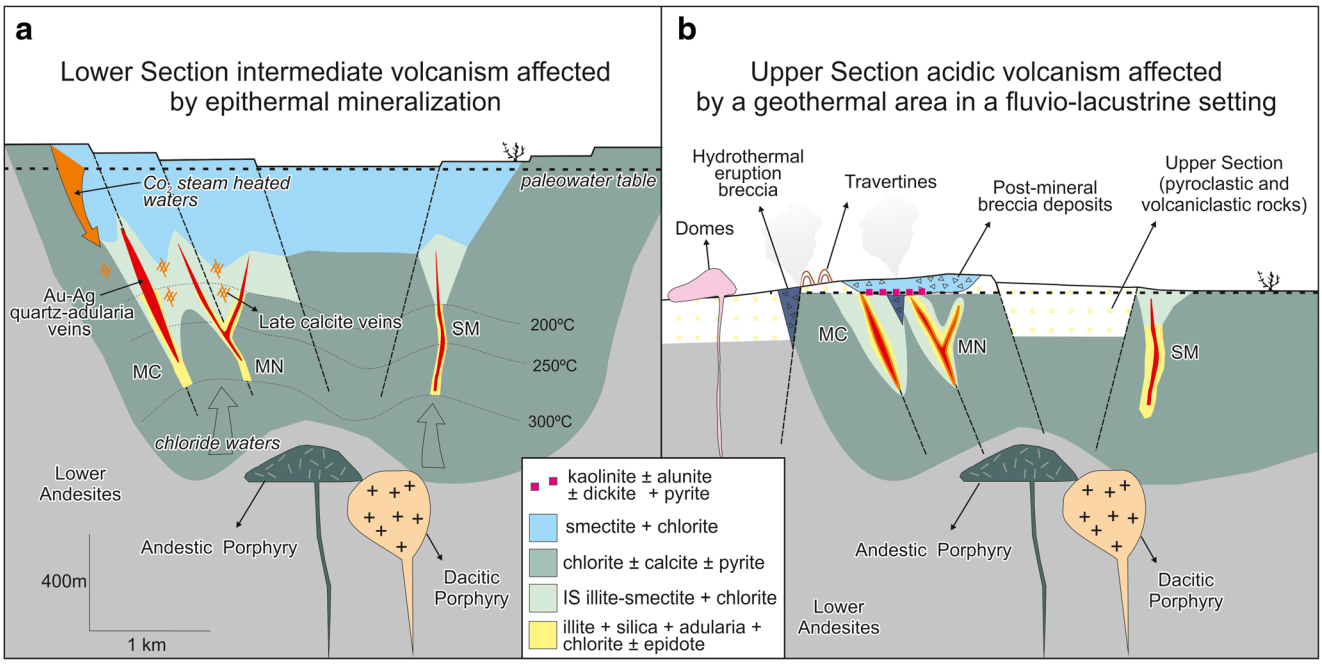

Fig. 12 Geologic and mineralization evolution for the Marianas-San Marcos vein system. **a** Formation of precious metal-bearing epithermal veins at ~155 Ma, related to late stages of the Lower Section units (157–156 Ma), and at a depth of formation of about 600 to 800 m below the paleowater table. **b** Upper Section acidic volcanism after uplift and erosion, with preservation of shallow hot spring features (travertines and hydrothermal breccias) overprinting deeper vein mineralization

al. (2007), and Morgan (2009) in active geothermal environments, and pointed out recently by Sillitoe (2015) as being characteristic of a fossil epithermal paleosurface. The advanced argillic alteration assemblage recorded at the base of the breccia deposits above the Mariana Central vein (Fig. 9) supports the interpretation that these breccias formed close to the paleosurface (Schoen et al. 1974; Ebert and Rye 1997; Simmons and Browne 2000).

A striking aspect of the Marianas-San Marcos vein system is the high temperatures recorded in fluid inclusions and hydrothermal alteration assemblages of the epithermal veins, which are not in agreement with the regional fossil geothermal setting of the Cerro Negro district. Figure 12 sketches the interpreted evolution of volcanism and hydrothermal activity for the Marianas-San Marcos vein system.

Figure 12a shows the interpreted setting during formation of high-grade epithermal veins during the waning stage Lower Section volcanism. Homogenization temperatures of FI from the main mineralization episode (E1, 155 Ma) range from 260 to 300 °C, in agreement with the alteration mineral assemblage, and evidence of boiling indicates deposition 600 to 800 m below the paleowater table (Haas 1971). Mineralization episode 2 is interpreted to have formed at similar conditions, based on evidence of boiling, but with a general decrease in metal contents. Finally, late calcite veins from E3, recording temperatures and salinities similar to E1, suggest similar condition associated with collapse of CO_2 steam-heated waters during the waning stage of the epithermal system (Simmons et al. 2000). Consequently, episodes 1, 2, and 3 probably formed at similar depth conditions, and probably at the same time.

Figure 12b shows a post-mineralization scheme (<155 Ma) with an interpreted telescoping model with possible paleowater table drop and uplift, favoring erosion and exhumation of the vein system, a common process in epithermal settings according to Sillitoe (1994, 2015). At this time, deposition of rhyolitic volcanic products of the Upper Section and related late geothermal features (hot spring and hydrothermal eruption breccia deposits) overprinted the earlier system. E4 could be related to this event, in which a silver-rich phase precipitated by remobilization at lower temperatures, as was observed by Páez et al. (2016) at the Martha mine.

Conclusion

The Marianas-San Marcos system consists of high-grade Au–Ag epithermal quartz veins hosted in steeply dipping normal faults associated with a Jurassic NW to EW half-graben structure. Veins have a Ag/Au ratio of about 10, low base metal content, and a complex infill history that can be summarized in four main episodes: a low volume, metal-rich initial episode (E1), an extended banded quartz episode with some metal input (E2), a barren waning stage episode (E3), and a silver-rich late tectonic–hydrothermal episode (E4).

The first three episodes are interpreted to have formed at the same time (~155 Ma), and probably from a fluid of the same composition (mixture of volcanic and meteoric waters at 290–230 °C, with <3 % NaCl equiv. salinity), closely related to the 157–156 Ma andesitic-dacitic shallow intrusions emplaced at the end of the intermediate Lower Section volcanic sequence. Metal was mainly precipitated at the beginning of vein formation (episode 1) due to a combination of boiling and mixing/cooling processes at approximately 600 to 800 m depth. Veins are considered to have characteristics of low to intermediate sulfidation systems, according to the epithermal system classifications of Hedenquist et al. (2000), Einaudi et al. (2003), Sillitoe and Hedenquist (2003), and Simmons et al. (2005).

Following deposition, the veins were uplifted and eroded, and partially covered by younger acidic volcanic deposits of the Upper Section, a volcanic sequence that ended with non-explosive formation of rhyolitic domes and reworked volcaniclastic materials, together with shallow geothermal features, as proposed by Guido and Campbell (2012). The last tectonic–hydrothermal mineralization episode (E4), interpreted to have formed at lower temperatures, could be related to this late tectonic and hydrothermal activity.

The Mariana-San Marcos vein system represents an outstanding example of telescoped epithermal deposits within the Deseado Massif. The presence of post-mineralization Jurassic volcanism, together with shallow epithermal features and overprinting and concealing high-grade Au–Ag veins, highlight the potential of finding buried high-grade mineralization below the widespread Jurassic fossil geothermal areas preserved in this region.

Acknowledgments This research was part of a PhD thesis carried out at the Universidad National de La Plata (UNLP) with the support of CONICET, UNLP, and Goldcorp Inc. mining company. We thank Gassaway Brown, Damián Echavarría, and the rest of the Cerro Negro staff for their assistance and access to data. We also want to thank Ramiro Lopez for permission to publish the U-Pb geochronology data from his unpublished PhD thesis. Finally, we appreciate the support given by Gerardo Páez, Kathy Campbell, Stuart Simmons, and Andreas Dietrich for very helpful comments and reviews.

References

Alric V, Haller M, Feraud G, Bertrand H, Zubia M (1996) Cronología 40Ar/39Ar del Vulcanismo Jurásico de la Patagonia Extraandina. XIII Congreso de Exploración de Hidrocarburos. Acta 5:243–251

Arribas A Jr, Schalamuk IB, de Barrio R, Fernández R, Itaya T (1996) Edades Radimétricas de Mineralizaciones Epitermales Auríferas del Macizo del Deseado, Provincia de Santa Cruz, Argentina. IGCP Project 342: age and isotopes of South American Ores. Acta XXXIX Congreso Bras Geol 6:254–257

Bodnar RJ (1993) Revised equation and table for determining the freezing point depression of H_2O-NaCl solutions. Geochim Cosmochim Acta 57:683–684

Bodnar RJ (2003) Introduction to aqueous fluid systems. In: Samson I, Anderson A Marshall D (eds) Fluid inclusions: analysis and interpretation. Mineral. Assoc. Canada, Short Course 32, 81–99

Bodnar RJ, Vityk MO (1994) Interpretation of microthermometric data for H2O–NaCl fluid inclusions. In: De Vivo B, Frezzotti ML (eds) Fluid inclusions in minerals, methods and applications. Virginia Tech, Blacksburg, pp 117–130

Bodnar RJ, Reynolds TJ, Kuehn CA (1985) Fluid-inclusion systematics in epithermal systems. Rev Econ Geol 2:73–97

Brathwaite RL, Faure K (2002) The Waihi epithermal gold-silver base metal sulfide quartz vein system, New Zealand: temperature and salinity controls on electrum and sulfide deposition. Econ Geol 97: 269–290

Brown KL (1986) Gold deposition from geothermal discharges in New Zealand. Econ Geol 81:979–983

Browne PRL, Ellis AJ (1970) The Ohaki-Broadlands geothermal area, New Zealand: mineralogy and related geochemistry. Am J Sci 269: 97–131

Browne PR, Lawless J (2001) Characteristics of hydrothermal eruptions, with examples from New Zealand and elsewhere. Earth Sci Rev 52: 299–331

Browne PRL, Courtney SF, Wood CP (1989) Formation of calc- silicate minerals deposited inside drillhole casing, Ngatamariki geothermal field, New Zealand. Am Mineral 74:759–763

Cas RAF, Wright JV (1988) Volcanic successions modern and ancient. Springer, Netherlands, **528p**

Channing A, Zamuner AB, Zúñiga A (2007) A new Middle–Late Jurassic flora and hot spring chert deposit from the Deseado Massif, Santa Cruz province, Argentina. Geol Mag 144:401–411

Christiansen RL, Lowenstern JB, Smith RB, Heasler H, Morgan LA, Nathenson M, Mastin LG, Muffler LJP, Robinson JE (2007) Preliminary assessment of volcanic and hydrothermal hazards in Yellowstone National Park and vicinity: U.S. Geological Survey Open-file Report 2007-1071, 94 p

Clayton RN, Mayeda T (1963) The use of bromine pentafluoride in the extraction of oxygen from oxides and silicates for isotopic analysis. Geochim Cosmochim Acta 27:47–52

Corbett G, Leach T (1997) Southwest pacific gold–copper systems: structure, alteration and mineralization. In: Corbett, Leach (Ed) Short Course Manual 225 pp

Cravero F, Domínguez E, Murray H (1991) Valores δ18O en caolinitas indicadoras de un clima templado húmedo para el Jurásico superior-Cretácico inferior de la Patagonia. Rev Asoc Geol Argent 46(1–2): 20–25

de Barrio R, Panza JL, Nullo F (1999) Jurásico y Cretácico del Macizo del Deseado, provincia de Santa Cruz. In: Caminos R (ed) Geol Argent 29 (17):511–527

Dietrich A, Gutierrez R, Nelson EP, Layer PW (2012) Geology of the epithermal Ag–Au Huevos Verdes vein system and San José district, Deseado massif, Patagonia, Argentina. Mineral Deposits 47(3):233–249

Dong G, Morrison GW, Jaireth S (1995) Quartz textures in epithermal veins, Queensland: classification, origin and implications. Econ Geol 90:1841–1856

Dubé B, Zubia M, Dunning G, Villeneuve M (2003) Estudio geocronológico de los campos filoneanos de baja sulfuración hospedados en la formación Chon Aike en el Macizo del Deseado, Provincia de Santa Cruz. In: Zubia M, Genini A (eds) Yacimientos auroargentíferos epitermales del Macizo del Deseado, Provincia de Santa Cruz. SEGEMAR Serie Contrib- uciones Técnicas Recursos Minerales 13/D, pp 17–24

Ebert S, Rye R (1997) Secondary precious metal enrichment by steam-heated fluids in the Crofoot-Lewis hot spring gold-silver deposit and relation to paleoclimate. Econ Geol 92:578–600

Echavarría LE, Schalamuk IB, Etcheverry RO (2005) Geologic and tectonic setting of Deseado Massif epithermal deposits, Argentina, based on El Dorado–Monserrat. J S Am Earth Sci 19:415–432

Echeveste H (2005) Travertines and jasperoids of the Manantial Espejo, a Jurassic hot spring environment. Macizo del Deseado, Santa Cruz province, Argentina. Lat Am J Sedimentol Basin Anal 12:23–39

Echeveste H, Fernandez R, Bellieni G, Tessone M, Llambias E, Schalamuk I, Piccirillo E, Demin A (2001) Relaciones entre las Formaciones Bajo Pobre y Chon Aike (Jurásico medio a superior) en el área de Estancia El Fénix–Cerro Huemul, zona centro-occidental del Macizo del Deseado, provincia de Santa Cruz. Rev Asoc Geol Argent 56(4):548–558

Einaudi MT, Hedenquist JW, Esra Inan E (2003) Sulfidation state of fluids in active and extinct hydrothermal systems: transitions from porphyry to epithermal environments. SEG Spec Pub 10:285–313

Faure K, Matsuhisa Y, Metsugi H, Mizota C, Hayashi S (2002) The Hishikari Au-Ag epithermal deposit, Japan: oxygen and hydrogen isotope evidence in determining the source of paleohydrothermal fluids. Econ Geol 97:481–498

Féraud G, Alric V, Fornari M, Bertrand H, Haller M (1999) $^{40}Ar/^{39}Ar$ dating of the Jurassic volcanic province of Patagonia: migrating magmatism related to Gondwana break-up and subduction. Earth Planet Sci Lett 172:83–96

Fernández RR, Blesa A, Moreira P, Echeveste H, Mykietiuk K, Andrada De Palomera P, Tessone M (2008) Los depósitos de oro y plata vinculados al magmatismo jurásico de la Patagonia: revisión y perspectivas para la exploración. Rev Asoc Geol Argent 63(4): 665–681

Feruglio E (1949) Descripción geológica de la Patagonia. 3 Volúmenes, Dirección Nacional de Yacimientos Petrolíferos Fiscales, Buenos Aires

Friedman I, O'Neil JR (1977) Compilation of stable isotope fractionation factors of geochemical interest: U.S. Geological Survey Professional Paper 440-KK: 12 p

Giacosa R, Zubia M, Sánchez M, Allard J (2010) Meso-Cenozoic tectonics of the southern Patagonian foreland: structural evolution and implications for Au–Ag veins in the eastern Deseado Region (Santa Cruz, Argentina). J S Am Earth Sci 30:134–150

Giggenbach WF (1992) Magma degassing and mineral deposition in hydrothermal systems along convergent plate boundaries. Econ Geol 87:1927–1944

Gilligan L, Marshall B (1987) Textural evidence for remobilization in metamorphic environments. Ore Geol Rev 2:205–229

Goldstein RH, Reynolds TJ (1994) Systematics of fluid inclusions in diagenetic minerals: SEPM Short Course Notes, 31: 199p

Gu L, Zheng Y, Tang X, Zaw K, Della-pasque F, Wu C, Tian Z, Lu J, Ni P, Li X, Yang F, Wang X (2007) Copper, gold and silver enrichment in ore mylonites within massive sulphide orebodies at Hongtoushan VHMS deposit, N.E. China. Ore Geol Rev 30:1–29

Guido D (2002) Geología y metalogénesis del sector oriental del Macizo del Deseado, provincia de Santa Cruz. PhD thesis, Universidad Nacional de La Plata, La Plata, Argentina, 226 pp. Available at: http://sedici.unlp.edu.ar/handle/10915/4617

Guido DM (2004) Subdivisión litofacial e interpretación del volcanismo jurásico (Grupo Bahía Laura) en el este del Macizo del Deseado, provincia de Santa Cruz. Rev Asoc Geol Argent 50:727–742

Guido DM, Campbell KA (2011) Jurassic hot spring deposits of the Deseado Massif (Patagonia, Argentina): characteristics and controls on regional distribution. J Volcanol Geotherm Res 203:35–47

Guido DM, Campbell KA (2012) Diverse subaerial and sublacustrine hot spring settings of the Cerro Negro epithermal system (Jurassic, Deseado Massif), Patagonia, Argentina. J Volcanol Geotherm Res 229–230:1–12

Guido DM, Campbell KA (2014) A large and complete Jurassic geothermal field at Claudia, Deseado Massif, Santa Cruz, Argentina. J Volcanol Geotherm Res 275:61–70

Guido DM, Schalamuk IB (2003) Genesis and exploration potential of epithermal deposits from the Deseado Massif, Argentinean Patagonia. In: Eliopoulos et al (eds) Mineral exploration and sustainable development. Balkema, Rotterdam, pp 493–496

Guido DM, De Barrio R, Schalamuk I (2002) La Marciana Jurassic sinter implications for exploration for epithermal precious-metal deposits in the Deseado Massif, southern Patagonia, Argentina. Trans Inst Min Metall 111:106–113

Guido DM, Escayola M, de Barrio RE, Schalamuk IB, Franz G (2006) La Formación Bajo Pobre (Jurásico) en el este del Macizo del Deseado, Patagonia Argentina: Vinculación con el Grupo Bahía Laura. Rev Asoc Geol Argent 61(2):187–196

Haas J (1971) The effect of salinity on the maximum thermal gradient of a hydrothermal system at hydrostatic pressure. Econ Geol 66:940–946

Hechem J, Homovc J (1987) Facies y paleoambientes volcaniclásticos en el Nesocratón del Deseado. Bol Informaciones Petroleras 16:2–23

Hedenquist JW, Henley RW (1985a) The importance of CO on freezing point measurements of fluid inclusions: evidence from active geothermal systems and implications for epithermal ore deposition. Econ Geol 80:1379–1406

Hedenquist JW, Henley RW (1985b) Hydrothermal eruptions in the Waiotapu geothermal system, New Zealand; their origin, associated breccias, and relation to precious metal mineralization. Econ Geol 80:1640–1668

Hedenquist JW, Lowenstern JB (1994) The role of magmas in the formation of hydrothermal ore deposits. Nature 370:519–527

Hedenquist JW, Izawa E, Arribas Jr A, White NC (1996) Epithermal gold deposits: styles, characteristics, and exploration. Poster and booklet, Resource Geology Spec Pub 1, 17 pp

Hedenquist J, Arribas R, Gonzalez Urien E (2000) Exploration for epithermal gold deposits. Econ Geol 13:245–277

Heinrich CA, Pettke T, Halter WE, Aigner-Torres M, Audétat A, Günther D, Hattendorf B, Bleiner D, Guillong M, Horn I (2003) Quantitative multi-element analysis of minerals, fluid and melt inclusions by laser-ablation inductively-coupled-plasma mass-spectrometry. Geochim Cosmochim Acta 67:3473–3497

Hobbs BE (1987) Principles involved in mobilization and remobilization. Ore Geol Rev 2:37–45

Jovic SM, Jovic NR, Guido DM, Schalamuk IB (2008) Caracterización de cuerpos intrusivos de la formación Cerro León en el área del Anticlinal el Tranquilo, Macizo del Deseado, Santa Cruz. XVII Congreso Geológico Argentino. Actas (2):851–852

Jovic SM, Guido DM, Schalamuk IB, Ríos FJ, Tassinari CCG, Recio C (2011) Pingüino In-bearing polymetallic vein deposit, Deseado Massif, Patagonia, Argentina: characteristics of mineralization and ore-forming fluids. Mineral Deposits 46:257–271

Lesta PJ, Ferello R (1972) Región extrandina de Chubut y Norte de Santa Cruz. In: Leanza AF (ed) Geología regional Argentina. Academia Nacional de Ciencias, Córdoba, pp 601–653

Lopez RG (2006) Estudio Geológico-Metalogenético del área oriental al curso medio del Río Pinturas, sector noroeste del Macizo del Deseado, provincia de Santa Cruz, Argentina. Ph.D. thesis, University of La Plata. p. 206

Lopez RG, Gómez JC, de Barrio RE, Schalamuk IB (2002) Lineaments analysis in epithermal deposits exploration, Southern Argentina. AIG J 114–117

Ludwig KY (2001). Isoplot/Ex, rev. 2.49, a geochronological toolkit for microsoft excel, Berkeley Geochronlogy Center Special Publication, 1a, 56 p

Marshall B, Gilligan L (1987) An introduction to remobilization: information from ore-body geometry and experimental considerations. Ore Geol Rev 2:87–131

Matsuhisa Y, Aoki M (1994) Temperature and oxygen isotope variations during formation of the Hishikari Epithermal gold-silver veins, southern Kyushu, Japan. Econ Geol 89:1608–1613

Moncada D, Bodnar RJ (2012) Gangue mineral textures and fluid inclusion characteristics of the Santa Margarita vein in the Guanajuato mining district, Mexico. Cent Eur J Geosci 4:300–309

Moncada D, Mutchler S, Nieto A, Reynolds TJ, Rimstidt JD, Bodnar RJ (2012) Mineral textures and fluid inclusion petrography of the epithermal Ag-Au deposits at Guanajuato, Mexico: application to exploration. J Geochem Explor 114:20–35

Moreira P (2005) Geología y metalogénesis del distrito La Josefina, macizo del Deseado, provincia de Santa Cruz PhD thesis, Universidad Nacional de La Plata, La Plata, Argentina, 360 pp. Available at: http://sedici.unlp.edu.ar/handle/10915/4478

Morgan L (2009) Hydrothermal processes above the Yellowstone magma chamber: large hydrothermal systems and large hydrothermal explosions. Geol Soc Am Special Paper 459

Mutchler SR, Fedele L, Bodnar RJ (2008) Analysis Management System (AMS) for reduction of laser ablation ICPMS data. In: Sylvester P (ed) Laser-ablation-ICPMS in the earth sciences: current practices and outstanding issues. Mineral Association of Canada. Short Course Series 40: 318–327

Nelson CE, Giles DL (1985) Hydrothermal eruption mechanisms and hot spring gold deposits. Econ Geol 80:1633–1639

O'Neil JR, Clayton RN, Mayeda TK (1969) Oxygen isotope fractionation in divalent metal carbonates. J Chem Phys 51:5547–5558

Ohmoto H, Rye RO (1979) Isotopes of sulfur and carbon. In: Barnes HL (ed) Geochemistry of hydrothermal ore deposits, 2nd edn. Wiley, New York, pp 509–567

Páez G, Ruiz R, Guido DM, Ríos FJ, Subias I, Recio C, Schalamuk I (2016) High-grade ore shoots at the Martha epithermal vein system, Deseado Massif, Argentina: the interplay of tectonic, hydrothermal and supergene processes in ore genesis. Ore Geol Rev 72:546–561

Pankhurst R, Leat P, Sruoga P, Rapela C, Marquez M, Storey B, Riley T (1998) The Chon Aike province of Patagonia and related rocks in West Antartica: a silicic large igneous province. J Volcanol Geotherm Res 81:113–136

Pankhurst R, Riley T, Fanning C, Kelley S (2000) Episodic silicic volcanism in Patagonia and the Antarctic Peninsula: chronology of magmatism associated with the Break-up of Gondwana. J Petrol 41:605–625

Panza JL, Haller MJ (2002) El volcanismo jurásico. In: Haller MJ (ed) Geología y recursos Naturales de Santa Cruz. Relatorio del XV Congreso Geológico Argentino. pp. 89–102

Passchier C, Trouw WY (2005) Microtectonics. Springer.371 p

Permuy Vidal C, Zalazar M, Guido DM, Brown G (2013) Evolution of the post-mineralization Marianas hydrothermal eruption breccia, Cerro Negro District, Patagonia, Argentina. In 35th New Zealand Geothermal Workshop: 2013 Proceedings, Rotorua, New Zealand. 6 p

Permuy Vidal C, Moreira P, Guido DM, Fanning C (2014) Linkages between the southern Patagonia Pre-Permian basements: new insights from detrital zircons U-Pb SHRIMP ages from the Cerro Negro District. Geol Acta 12(2):137–150

Ramos V (2002) Evolución tectónica. In: M. Haller (ed) Geología y Recursos Naturales de Santa Cruz. Relatorio del XV Congreso Geológico Argentino. El Calafate, I-23:235–387

Richardson N, Underhill JR (2002) Controls on the structural architecture and sedimentary character of syn-rift sequences, North Falkland Basin, South Atlantic. Mar Pet Geol 19:417–443

Riley TR, Leat PT, Pankhurst RJ, Harris C (2001) Origins of large volume rhyolitic volcanism in the Antarctic Peninsula and Patagonia by crustal melting. J Petrol 42:1043–1065

Roedder E (1984) Fluid inclusions. Rev in Mineral 12:644 p

Ruiz R (2012) Geología y Mineralizaciones del sector sudoccidental del Macizo del Deseado, Santa Cruz PhD thesis, Universidad Nacional

de La Plata, La Plata, Argentina. 314 pp. Available at http://sedici.unlp.edu.ar/handle/10915/25786

Sander MV, Black JE (1988) Crystallization and recrystallization of growth-zoned vein quartz crystals from epithermal systems; implications for fluid inclusion studies. Econ Geol 83(5):1052–1060

Sawkins FJ, O'Neil JR, Thompson JM (1979) Fluid inclusion and geochemical studies of vein gold deposits, Baguio district, Philippines. Econ Geol 74:1420–1434

Schalamuk IB, Zubia M, Genini A, Fernández R (1997) Jurassic epithermal Au-Ag deposits of Patagonia, Argentina. Ore Geol Rev 12(3):173–186

Schalamuk IB, de Barrio R, Zubia M, Genini A, Echeveste H (1999) Provincia Auroargentífera del Deseado, Santa Cruz. Recursos Minerales de la República Argentina In: Zappettini E (ed) Instituto de Geología y Recursos Minerales SEGEMAR, Anales, 35: 177–1188

Schalamuk IB, de Barrio RE, Zubia MA, Genini A (2002) Mineralizaciones auro-argentíferas del Macizo del Deseado y su enfoque metalogénico. In: Haller MJ (Ed) Geología y Recursos Naturales de Santa Cruz, Relatorio del XV Congreso Geológico Argentino, pp. 679–713 (Buenos Aires)

Schoen R, White DE, Hemley JJ (1974) Argillization by descending acid at the Steamboat Springs, Nevada. Clay Clay Miner 22:1–22

Sharpe R, Riveros C, Scavuzzo V (2002) Stratigraphy of the Chon Aike formation ignimbrite sequence in the Cerro Vanguardia Au-Ag epithermal vein district. XV Congreso Geológico Argentino Actas

Shatwell D, Clifford JA, Echavarría D, Irusta G, Lopez D (2011) Discoveries of low-sulfidation epithermal Au–Ag veins at Cerro Negro, Deseado Massif, Argentina. SEG Newsl 85:16–23

Sheppard SMF, Gilg HA (1996) Stable isotope geochemistry of clay minerals. Clay Miner 31:1–24

Sigurdsson H, Houghton B, McNutt S, Rymer H, Stix J (Eds) (2015) The encyclopedia of volcanoes, 2nd edn. Elsevier, 1456 p

Sillitoe EH (1994) Erosion and collapse of volcanoes: causes of telescoping in intrusion-centered ore deposits. Geology 22:945–948

Sillitoe EH (2015) Epithermal paleosurfaces. Mineral Deposita 50:767–793

Sillitoe RH, Hedenquist JW (2003) Linkages between volcanotectonic settings, ore-fluid compositions, and epithermal precious metal deposits. SEG Spec Pub 10:315–343

Simmons S, Browne PR (2000) Hydrothermal minerals and precious metals in the Broadlands-Ohaaki geothermal system: implications for understanding low-sulfidation epithermal environments. Econ Geol 95:971–999

Simmons SF, Christenson BW (1994) Origins of calcite in a boiling geothermal system. Am J Sci 294:361–400

Simmons SF, Arehart G, Simpson MP, Mauk JL (2000) Origin of massive calcite veins in the golden cross low-sulfidation, epithermal Au-Ag deposit, New Zealand. Econ Geol 95:99–112

Simmons S, White N, John D (2005) Geological characteristics of epithermal precious and base metal deposits. SEG 100th anniversary volume, pp 485–522

Simpson MP, Mauk JL (2011) Hydrothermal alteration and veins at the epithermal Au-Ag deposits and prospects of the Waitekauri Area, Hauraki Goldfield, New Zealand. Econ Geol 106:945–973

Simpson MP, Palinkas SS, Mauk JL, Bodnar RJ (2015) Fluid inclusion chemistry of Adularia-Sericite epithermal Au-Ag deposits of the Southern Hauraki Goldfield, New Zealand. Econ Geol 110:763–786

Taylor BE (1986) Magmatic volatiles: isotopic variations of C, H, and S. Rev Mineral 16:185–225

Ueda A, Roy Cruise H (1986) Direct conversion of sulphide and sulphate minerals to SO2 for isotope analysis. Geochem J 20:209–212

Vaughan DJ, Craig JR (1997) Sulfide ore mineral stability, morphologies, and intergowth textures. In: Barnes HL (ed) Geochemistry of hydrothermal ore deposits, 3rd edn. Wiley, p. 367–434

Wallier S (2009) The geology and evolution of the Manantial Espejo epithermal silver (+gold) deposit, Deseado Massif, Argentina. Unpublished PhD Thesis. University of British Columbia, Vancouver, Canada. 303 pp. Available at http://circle.ubc.ca/handle/2429/17439

Zheng YF (1993) Calculation of oxygen isotope fractionation in hydroxyl-bearing silicates. Earth Planet Sci Lett 120:247–263